Roger Wördenweber, Victor Moshchalkov, Simon Bending and Francesco Tafuri

Superconductors at the Nanoscale

Also of Interest

Nano Devices and Sensors
Juin J. Liou, Shien-Kuei Liaw, Yung-Hui Chung, 2016
ISBN 978-1-5015-1050-2, e-ISBN 978-1-5015-0153-1

Structures on Time Scales
Theo Woike, Dominik Schaniel, 2017
ISBN 978-3-11-044209-0, e-ISBN 978-3-11-043392-0

Computational Strong-Field Quantum Dynamics. Intense Light-Matter Interactions
Dieter Bauer, 2017
ISBN 978-3-11-041725-8, e-ISBN 978-3-11-041726-5

Zeitschrift für Naturforschung A. A Journal of Physical Sciences
Martin Holthaus (Editor-in-Chief)
ISSN 0932-0784, e-ISSN 1865-7109

Superconductors at the Nanoscale

From Basic Research to Applications

Edited by
Roger Wördenweber, Victor Moshchalkov, Simon Bending
and Francesco Tafuri

EUROPEAN COOPERATION
IN SCIENCE & TECHNOLOGY

Funded by the Horizon 2020 Framework Programme
of the European Union

DE GRUYTER

Editors

Prof. Dr. Roger Wördenweber
Forschungszentrum Jülich
Peter Grünberg Institut (PGI-8)
52425 Jülich
Germany
r.woerdenweber@fz-juelich.de

Prof. Victor Moshchalkov
KU Leuven
Institute for Nanoscale Physics
and Chemistry
Celestijnenlaan 200D
3001 Heverlee
Belgium
victor.moshchalkov@fys.kuleuven.be

Prof. Simon Bending
University of Bath
School of Physics
Claverton Down
Bath Ba2 7AY
United Kingdom
pyssb@bath.ac.uk

Prof. Francesco Tafuri
Seconda Università di Napoli
Via Roma 29
81031 Aversa
Italy
tafuri@na.infn.it

Cover Image: Artistic 3D view (realized by Dr. T. Cren – INSP, Sorbonne Universités, CNRS, Paris, France) of quantum vortices in superconducting nano-islands of Pb subject to a magnetic field. Individual Abrikosov-Pearl vortices appear as regular dark spots inside the islands and the Josephson ones in between (see D. Roditchev, et al. Nature Phys. 11, 332 (2015) and Chapter 3 in this book: *STM studies of vortex cores in strongly confined nanoscale superconductors*).

ISBN 978-3-11-045620-2
e-ISBN (PDF) 978-3-11-045680-6
e-ISBN (EPUB) 978-3-11-045624-0

Library of Congress Cataloging-in-Publication Data
A CIP catalog record for this book has been applied for at the Library of Congress.

Bibliographic information published by the Deutsche Nationalbibliothek
The Deutsche Nationalbibliothek lists this publication in the Deutsche Nationalbibliografie; detailed bibliographic data are available on the Internet at http://dnb.dnb.de.

Cover image: Drs. Ch. Brun, T. Cren, and D. Roditchev – INSP, Sorbonne Universités, CNRS, Paris, France
Typesetting: le-tex publishing services GmbH, Leipzig
Printing and binding: Hubert & Co. GmbH & Co. KG, Göttingen
♾ Printed on acid-free paper
Printed in Germany

www.degruyter.com

Contents

Foreword

The enigmatic problem of *“perpetuum mobile”* has attracted a lot of attention over the years, starting already in the Middle Ages. Indeed, *perpetual* motion implies a lack of energy dissipation which is a very unusual situation in science. Two key cases of nondissipating motion on a macroscopic scale are well known:
– the *flow of electrical current in superconductors* and
– the *propagation of light* (and other electromagnetic waves as well) *in vacuum*.

If a current is induced in a superconducting ring that is meters or kilometers in size, it circulates there forever. When we enjoy the romantic glimmer of a distant star in the night, the light from it has arrived after traveling for billions of years, a nice experimental proof of dissipation-free propagation. An important difference here is that the first system deals with current in *condensed matter,* the second one with the propagation of electromagnetic fields in *vacuum*. In the first case, the energy dissipation is forbidden by the existence of the coherent *quantum* state of the condensate of the charged Cooper pairs carrying the current, while in the second case there is not too much to interact with for the light propagating in vacuum, as prescribed by the *classical* Maxwell’s equations.

Whereas propagating light interacts with matter or gravitational waves and represents the basis for optical devices and experiments, the *frictionless flow of supercurrent* interferes with *nanosize objects* in the superconductor such as tunnel barriers, surfaces, interfaces, or the so-called *fluxons* or *vortices*, quantized magnetic flux of extremely small magnitude $\Phi_0 = h/2e \approx 2.06 \times 10^{-15}$ Wb, that are induced by an applied current, a magnetic field, or thermal fluctuations. On the one hand, an appropriate nanotechnology is required to master *fluxon behavior* – for instance through designing appropriate pinning potentials to localize the fluxons (vortices) – and retain the frictionless supercurrent that is necessary for a number of superconducting applications. This forms one of the main objectives of *fluxonics*. On the other hand, it offers a wide range of options for improved or even novel fluxonic concepts, especially since the necessary tools for “nanoengineering” superconducting materials are readily available nowadays.

Generally, the superconducting condensate is described by the “order parameter” that obeys the Ginzburg–Landau (GL) equations (*Nobel Prize in Physics, 2003*). The boundary conditions for these, strongly influencing the solutions, are imposed at the physical sample boundaries, thus implying that the properties of confined fluxons can be tailored by applying specific surface configurations. This creates a unique opportunity for the *“quantum design” of the physical properties of the confined condensates and fluxons* through the application of specially defined nanomodulated boundary conditions, which can be additionally tuned using, for instance, magnetic templates, electrical fields, or even optical signals. The imposed nanomodulation can therefore lead to the practical implementation of the confined fluxon patterns possessing the specific properties needed for applications in fluxonics ranging from passive and active elements to qubits for quantum computing.

It is the intention of this book to highlight and discuss the state-of-the-art and recent progress in this field, as well as to highlight current problems with "Superconductors at the Nanoscale". This includes:

– the visualization and understanding of fluxons (vortices) and their interaction on the nanoscale, in nanostructured superconductors, as well as in novel types of superconductors;
– progress in controlling *static* fluxon configurations as well as the *dynamic* properties (up to THz frequencies) of fluxons in nanoscale superconductors;
– the behavior of different types of fluxons (Abrikosov vortices, kinematic vortices, and Josephson vortices) in mesoscopic, nanostructured, and/or layered superconductors;
– the impact of the combination of superconductors with other materials, like ferromagnetic layers, on the nanoscale, and;
– progress in nanoscale superconducting electronics such as SQUIDs, THz emitters, or photonic detectors.

For a better general understanding, the topic of superconductivity is introduced in an extended Tutorial that provides a brief history and a scientific overview of the physics of superconductivity.

Victor V. Moshchalkov   Roger Wördenweber

Acknowledgment: This book is based upon work from COST Action "Nanoscale Superconductivity: Novel Functionalities through Optimized Confinement of Condensate and Fields" (NanoSC – COST Action MP1201), supported by COST (European Cooperation in Science and Technology).

COST (European Cooperation in Science and Technology) is a pan-European intergovernmental framework. Its mission is to enable break-through scientific and technological developments leading to new concepts and products and thereby contribute to strengthening Europe's research and innovation capacities. It allows researchers, engineers, and scholars to jointly develop their own ideas and take new initiatives across all fields of science and technology, while promoting multi- and interdisciplinary approaches. COST aims at fostering a better integration of less research intensive countries to the knowledge hubs of the European Research Area. The COST Association, an International not-for-profit Association under Belgian Law, integrates all management, governing, and administrative functions necessary for the operation of the framework. The COST Association has currently 36 Member Countries. www.cost.eu

Roger Wördenweber and Johan Vanacken

Tutorial on nanostructured superconductors

1 Introduction

Superconductivity represents an extraordinary phenomenon. In the superconducting state the material not only exhibits no electric resistance to an applied DC current, it shows also unique properties in magnetic fields that can be used for a large variety of applications ranging from energy production and management, medical diagnostics, to sensor and information technology. For a long time the application of superconductivity was hampered by its low transition temperature T_c that required cooling down to liquid He temperature at 4.2 K. As a consequence, superconductive solutions were considered and developed in the past only if classical solutions were not feasible. This was (and still is) the case for medical applications like magnetic resonance imaging (MRI) or electroencephalography, particle accelerators, and special detectors (e.g., bolometers or highly sensitive magnetic field detectors).

With the discovery of the so-called high-T_c materials with T_c values of 90 K and higher (see Figure 1), this situation has changed. Now it was possible to attain the superconducting state with much cheaper cooling by liquid nitrogen. However, it soon turned out that the new superconductors (i) have a very complex crystallographic structure, (ii) are highly anisotropic (2D superconductivity), and (iii) possess superconducting parameters that allow even smallest inhomogeneities to reduce or even destroy the superconductivity locally.

As a result, it is essential to analyze, understand and, if possible, optimize superconductors at the nanoscale. This includes among others a detailed study of the nanostructure of these superconductors, the resulting 'nanophysics', and the impact of nanostructures introduced by nanopatterning on the superconducting properties. This book represents a detailed report on this activity that was performed in the framework of a European project, the COST Action MP1201 '*Nanoscale Superconductivity (NanoSC), Novel Functionalities through Optimized Confinement of Condensate and Fields*'.

2 A brief history of superconductivity

In 1908, Kamerlingh Onnes [1] succeeded in the liquefaction of helium with a boiling point of 4.2 K at atmospheric pressure. Since the boiling point can be reduced by pressure reduction, he was now able to extend the experimentally available tempera-

DOI 10.1515/9783110456806-001,

ture range towards absolute zero. Using this opportunity, he started an investigation of the electric resistance of metals. At that time, it was known that electrons are responsible for charge transport. However, different ideas about the mechanism of the electric conduction and the resulting temperature dependence of the resistance were discussed:

1. At low temperature the crystal lattice 'freezes' and the electrons are not scattered any longer. As a consequence the resistance of all metals would approach zero with decreasing temperature (Dewar, 1904).
2. Similar to option 1, however due to impurities in the lattice, the resistance would approach a finite limiting value (Matthiesen, 1864).
3. In contrast to option 1 and 2, the electrons could be 'frozen' (i.e., bound to their respective atoms) at low temperature. Consequently, the resistance would pass through a minimum and approach infinity at very low temperatures (Lord Kelvin, 1902).

Initially, Kamerlingh Onnes studied platinum and gold samples, which he could obtain already with high purity. He found that the experiment agreed with the second option. At zero temperature the electric resistance of these samples saturated at a finite limiting value, the so-called residual resistance, that depended upon the purity of the samples. The purer the samples, the smaller the residual resistance. However, Kamerlingh Onnes expected that, ideally, pure platinum or gold should have a vanishingly small resistance (first option).

In order to test this hypothesis, Kamerlingh Onnes decided to study mercury, the only metal that at that time could be highly purified via multiple distillation processes. He expected that the resistance of pure mercury would hardly be measurable at 4.2 K and that it would gradually approach zero resistance at even lower temperatures. The initial experiments seemed to confirm these concepts, i.e., below 4.2 K the resistance of mercury became immeasurably small (see Figure 1). However, he soon recognized that the observed effect could not be identified with the expected decrease of resistance. The resistance change resembled more a resistance jump within a few hundredths of a Kelvin than a continuous decrease (see Figure 1). Therefore, Kamerlingh Onnes stated that '*At this point* (slightly below 4.2 K) ... *Mercury had passed into a new state, which on account of its extraordinary electrical properties may be called the superconductive state*' [2]. The new phenomenon was discovered and named superconductivity.

Meanwhile we know that superconductivity represents a widespread phenomenon. Many elements of the periodic system are superconductors (with Nb representing the element with the highest T_c of about 9.2 K) and thousands of superconducting compounds have been discovered in the meantime ranging from metallic compounds and oxides, to organic molecules (see Figure 1).

For the first 75 years, superconductivity represented a low-temperature phenomenon with the highest T_c of about 23.2 K in the A15 compound Nb_3Ge. In 1986

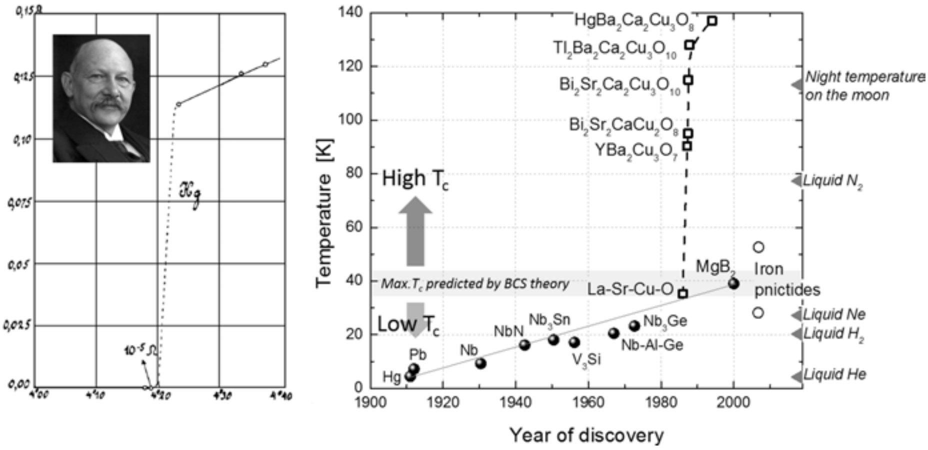

Fig. 1: Superconductivity of mercury (copy of the original figure from Kamerlingh Onnes [image in the figure]) and the evolution of the superconducting transition temperature T_c with time.

this changed, when Bednorz and Müller discovered superconductivity with a T_c in the range of 30 K in the copper-oxide system Ba-La-Cu-O [3]. This immediately started a 'rush' for new superconductors with even higher T_c's. Already in 1987, transition temperatures above 80 K were observed in the Y-Ba-Cu-O system [4]. During this time, new results more often were reported in press conferences than in scientific journals, the media carefully reported on these developments since superconductivity at temperatures above the boiling point of liquid nitrogen ($T = 77$ K) suggested many possible technical applications for this phenomenon.

Today, a large number of different Cu-O based (cuprate) superconductors with high transition temperatures are known, the so called 'high-T_c superconductors'. The most studied high-T_c cuprates are $YBa_2Cu_3O_7$ (YBCO), their rare earth counterparts $ReBa_2Cu_3O_7$ (with Re = Sc, Ce, La, Nd, Sm, Eu, Gd, Dy, Ho, Er, Tm, Yb, Lu), and $Bi_2Sr_2CaCu_2O_8$ (BSCCO or Bi2212) with transition temperatures slightly above 90 K. The record T_c value is presently that of $HgBa_2Ca_2Cu_3O_8$, with a T_c of 135 K or 164 K at atmospheric pressure or a pressure of 30 GPa, respectively.

Surprisingly, only in 2000 superconductivity with a T_c of 39 K was detected in MgB_2, even though this compound represents a 'classical' metallic superconductor and had already been commercially available for a long time [5]. In 2008 superconductivity was detected in quite exotic compounds, the so-called iron pnictides [6]. In analogy to the copper oxide layers in the cuprates, in these material FeAs layers form the basic building block for the superconductivity. Compositions like $LaFeAsO_{1-x}F_x$, $Ba_{1-x}K_xFe_2As_2$, or $ReFeAsO_{1-x}$ (with Re = Sm, Nd, Pr, Ce, La) show impressive T_c's up to 55 K. Finally, a large number of organic molecules also become superconducting at low temperature. Already in 1979 K. Bechgaard synthesized the first organic superconductor, $(TMTSF)_2PF_6$, with a T_c of 1.1 K at a pressure of 6.5 kbar. The corresponding material class was later named after him. Nowadays, transition temperatures of up to 33 K (2007, alkali-doped fullerene $RbCs_2C_{60}$) have been achieved. Organic superconductors are of special interest since they can form quasi-2D or even quasi-1D structures like Fabre or Bechgaard salts (e.g., κ-BEDT-TTF_2X or λ-$BETS_2X$ compounds), or graphite intercalation compounds.

This brief survey of superconductivity demonstrates that there has been a tremendous improvement of the transition temperature in the past years, which, however, is accompanied by a higher complexity and anisotropy of the material. The analysis, understanding, and optimization of the superconductivity in these materials clearly has to happen at the nanoscale.

3 Specific properties of superconductors

The most prominent property of the superconducting state is definitely the disappearance of the DC electric resistance (see Figure 1). The superconductor becomes an *ideal conductor*.

However, just as important is the behavior of the superconductor in magnetic fields. In 1933 Meissner and Ochsenfeld discovered that an externally applied magnetic field can be expelled from the interior of a superconductor (Figure 2), i.e., the superconductor can also act as an *ideal diamagnet* [28]. This can nicely be demonstrated in levitation experiments and represents the basis for levitation applications of superconductivity like levitation trains or magnetic bearings (Figure 2). Generally, the Meissner–Ochsenfeld effect is very surprising, since according to the induction law an ideal conductor is expected to preserve an interior constant magnetic field but not expel it. As will be shown later in this tutorial (Section 4.3), the behavior of a superconductor in a magnetic field is far more complex. It represents one of the major themes of this book.

4 Theoretical understanding

4.1 Microscopic approach of Bardeen, Cooper, and Schrieffer

The explanation for the unusual behavior of superconductors came with the BCS theory that was introduced by Bardeen, Cooper, and Schrieffer in 1957 [7]. They recognized that at the transition to the superconducting state, electrons (fermions) pairwise condense to a bosonic state, in which they form a coherent matter wave with a well-defined quantum-mechanic phase, the so-called Bose–Einstein condensate (the latter explains the Josephson effect that is introduced in the next section). They assumed that the interaction of the electrons is mediated by vibrations of the crystal lattice, i.e.,

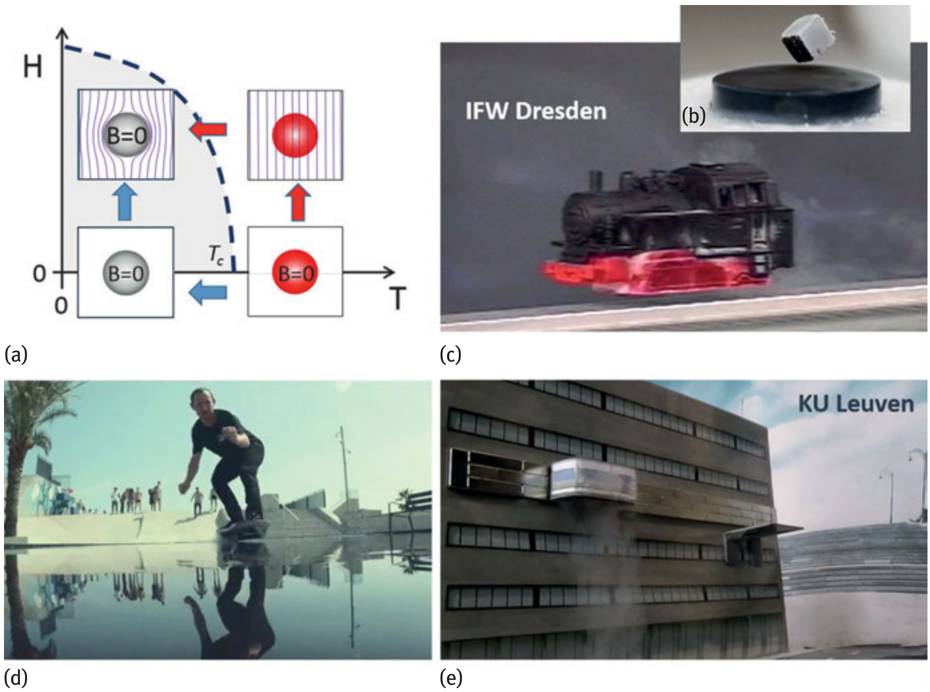

Fig. 2: (a) H-T phase diagram showing how a magnetic field interacts with a superconductor. In the normal state at high temperatures, a magnetic field simply penetrates the material. In the superconducting state below T_c, the perfect diamagnetism (blue arrows) will assure that the magnetic induction $B = 0$ inside the superconductor. However, even if the material is cooled in an applied magnetic field (red arrows), the superconductor expels the applied field. Both effects are manifestations of the Meissner–Ochsenfeld effect, that, among others, can be used for the levitation of a superconductor in a magnetic field. The latter is illustrated by: (b) laboratory demonstration using a liquid nitrogen cooled high-T_c superconductor and a magnet, (c) a 'toy train' of the IFW Dresden equipped with a superconducting pellet, hovering above a magnetic track, and (d) Toyota/Lexus using the same technology to make "back-to-the-future" real. (e) Because of pinning (see later), it is even possible to make a tram "levitate" along a building or upside down as shown by this model at the KU Leuven.

phonons. The resulting electron pairs are called *Cooper pairs*. In most cases, the spins of the two electrons align antiparallel (spin singlets) and the angular momentum of the pair is zero (s-wave).

The Cooper pairs behave differently from single electrons which are fermions and have to obey the Pauli exclusion principle. In contrast, Cooper pairs are bosons. They condense into a single energy level which is slightly lower (a few meV, see Table 1) than the energy level of the normal state. Therefore an energy gap 2Δ separates the unpaired electrons (the so-called quasiparticles) from the Cooper pairs (Figure 3a). The energy gap automatically explains (i) the DC zero-resistance of the superconduc-

Table 1: Critical temperature T_c and zero temperature values of the energy gap Δ, Ginzburg–Landau coherence length ξ_{GL}, and critical fields B_c (for type-I superconductors) and B_{c2} (for type-II superconductors). Since the values vary in the literature, they should be taken as a guide only. For anisotropic superconductors, the subscripts (ab) and (c) refer to in-plane and out-of-plane properties, respectively. The subscript 'max' indicates the maximum reported value.

Material	T_c (K)	Δ (meV)	ξ_{GL} (nm)	λ_L (nm)	B_c, B_{c2} (T)
Al	1.2	0.17	1600	34	0.01 (B_c)
Pb	7.2	1.38	51–83	32–39	0.08 (B_c)
Nb	9.2	1.45	40	32–44	0.2 (B_c)
NbN	13–16	2.4–3.2	4	250	16
Nb_3Sn	18	3.3	4	80	24
Nb_3Ge	23.2	3.9–4.2	3–4	80	38
NbTi	9.6	1.1–1.4	4	60	16
$YBa_2Cu_3O_7$	92	15–25 (max, ab)	1.6 (ab) 0.3 (c)	150 (ab) 800 (c)	240 (ab) 110 (c)
$Bi_2Sr_2CaCu_2O_8$	94	15–25 (max, ab)	2 (ab) 0.1 (c)	200–300 (ab) > 15000 (c)	> 60 (ab) > 250 (c)
$Bi_2Sr_2Ca_2Cu_3O_{10}$	110	25–35 (max, ab)	2.9 (ab) 0.1 (c)	150 (ab) > 1000 (c)	40 (ab) > 250 (c)
MgB_2	40	1.8–7.5	10 (ab) 2 (c)	110 (ab) 280 (c)	15–20 (ab) 3 (c)
$Ba_{0.6}K_{0.4}Fe_2As_3$	38	4–12	1.5 (ab) c > 5 (c)	190 (ab) 0.9 (c)	70–235 (ab) 100–140 (c)
$NdO_{0.82}F_{0.18}FeAs$	50	37	3.7 (ab) 0.9 (c)	190 (ab)c > 6000 (c)	62–70 (ab) 300 (c)

tor and (ii) the transition temperature, critical field, and other phenomena that restrict the superconducting regime, since it always requires an energy (thermal energy, magnetic field, current, or irradiation) of at least 2Δ to break a Cooper pair.

The BCS theory provides a number of valuable predictions. For instance, these include the temperature dependence of the energy gap (Figure 3c), the value of the energy gap at zero-temperature [9]:

$$\Delta\,(0\,\mathrm{K}) = 1.764 k_B T_c\,, \tag{1}$$

and the dependence of the superconducting transition temperature T_c on the electron-phonon interaction V and the Debye frequency ω_D which, in the simplest form, is given by [7]

$$k_B T = 1.13 \hbar \omega_D e^{-1/N(E_F)V}\,, \tag{2}$$

with k_B representing the Boltzmann constant and $N(E_F)$ the electronic density of states at the Fermi level. In the past, the latter equation suggested a possibility to optimize the transition temperature.

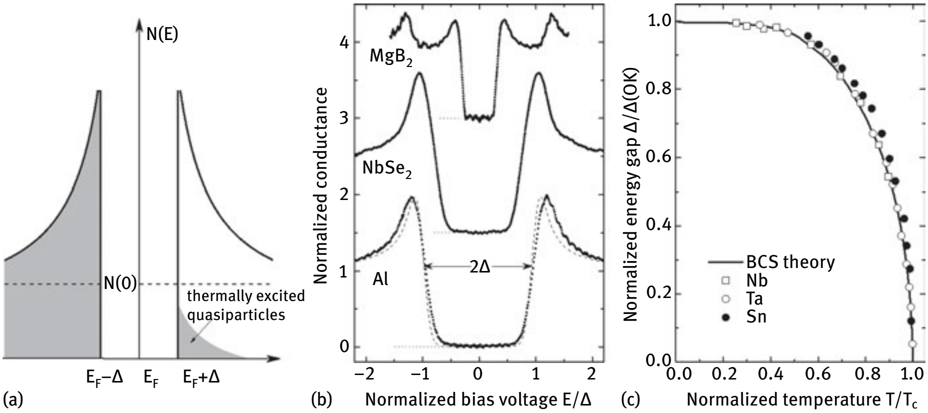

Fig. 3: (a) Schematic of the density of states at the superconducting energy gap, the shaded regime indicates the occupied states; (b) experimental verification obtained via scanning tunneling microscopy on various superconductors (see also Chapter 1), and (c) energy gap as function of reduced temperature according to the BCS theory (solid line) and for BCS-type superconductors (data from [8]). In (b) the data are normalized with respect to the energy gap Δ and, for better visibility, they are shifted with respect to the ordinate (gray dotted line represents zero conductance). Al and $NbSe_2$ show the 'classic' BCS behavior (for Al a BCS fit is added, dashed line), whereas MgB_2 represents a more complex superconductor with among others two energy gaps. For details of the tunnel spectroscopy and related topics refer to Chapter 1.

Many superconductors represent BCS-type superconductors (see Figure 3c) and even for the 'non-BCS-type superconductors' the general principles of the BCS theory are still valid. Nevertheless, we know now that the superconducting state can be much more complicated. This is especially the case for the much more complex new superconductors, like the high-T_c cuprates, MgB_2 (see Figure 3), pnictides, or even organic superconductors. Not only does Cooper pairing not really involve individual electrons pairing to form 'quasibosons', holes can also condensate to Cooper pairs, and d-wave superconductivity, p-wave superconductivity, multiband superconductivity, and coupling mechanisms other than phonon-mediated electron-electron interaction have to be taken into consideration to explain superconductivity in the more and more 'exotic' compounds. The careful analysis of the band structure of these materials is therefore a vital tool to understand these superconductors. A detailed discussion of this topic is given in Chapter 1.

4.2 Thermodynamic approach of Ginzburg and Landau

In contrast to the microscopic approach of the BCS theory, Ginzburg and Landau proposed a macroscopic description of superconductivity using universal thermodynamic arguments [10]. Their phenomenological theory was essentially correct when they presented it in 1950 (i.e., prior to the BCS theory), however they assumed a charge $q = e$ of the superconducting charge carrier. With the appearance of the BCS theory, this charge was then replaced by the charge of the Cooper pair, $q = 2e$. Later, in 1959, Gor'kov demonstrated that the Ginsburg–Landau theory can be derived from the BCS theory [11].

Based on Landau's previously thermodynamic description of 2nd order phase transitions, Ginzburg and Landau argued that the free energy F of a superconductor near the superconducting transition can be expressed in terms of a complex order parameter ψ, which is zero in the normal state and nonzero in the superconducting state. Furthermore, ψ is related to the density of the superconducting charge n_s. Assuming that $|\psi|$ is small, the free energy can be expressed by

$$F - F_n = \alpha|\psi|^2 + \frac{\beta}{2}|\psi|^4 + \frac{1}{2m}\left|\left(\frac{\hbar}{i}\nabla - 2e\boldsymbol{A}\right)\psi\right|^2 + \frac{|\boldsymbol{B}|^2}{2\mu_0}\,, \tag{3}$$

with the parameters F_n representing the free energy in the normal phase, the phenomenological parameters α and β, m and $2e$ the effective mass and charge of the Cooper pair, and $\boldsymbol{A}$ and $\boldsymbol{B}$ the magnetic vector potential and magnetic field, respectively. Minimizing the free energy with respect to variations in the order parameter and the vector potential yields the important *Ginzburg–Landau equations*

$$\begin{aligned} &\alpha\psi + \beta|\psi|^2\psi + \frac{1}{2m}\left(\frac{\hbar}{i}\nabla - 2e\boldsymbol{A}\right)^2\psi = 0\,, \\ &\boldsymbol{j} = \frac{1}{\mu_0}(\nabla\times\boldsymbol{B}) = \frac{2e}{m}\mathrm{Re}\left\{\psi * \left(\frac{\hbar}{i}\nabla + 2e\boldsymbol{A}\right)\psi\right\}\,, \end{aligned} \tag{4}$$

where $\boldsymbol{j}$ denotes the electric current density and Re the real part. The first equation resembles the time-independent Schrödinger equation except for the nonlinear term. It determines the order parameter ψ, whereas the second equation provides the superconducting current.

The Ginzburg–Landau equations predict two important characteristic lengths in a superconductor, the coherence length ξ_{GL} and the penetration depth λ. The coherence length

$$\xi_{GL} = \sqrt{\frac{\hbar}{2m|\alpha|}} \tag{5}$$

characterizes the thermodynamic fluctuations in the superconducting phase. It is for instance manifested at a superconductor surface where the density n_s of Cooper pairs vanishes exponentially with a length scale of ξ_{GL} (Figure 4). Obviously, this parameter is temperature dependent. Moreover, it is correlated to the so-called BCS coherence length $\xi_0 = \hbar v_F / k_B T_c$ which characterizes the distance over which the two electrons forming a Cooper pair are correlated. Here v_F denotes the Fermi velocity.

The second parameter, the London penetration length λ, was already introduced by the London brothers in 1935 [29]. Expressed in terms of the Ginzburg–Landau model

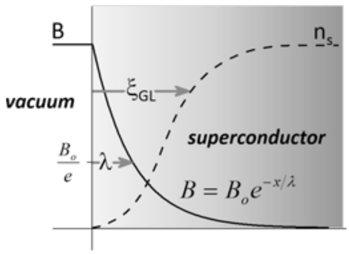

Fig. 4: Exponential decrease of the magnetic field and increase of the Cooper pair density at the surface of a superconductor define the London penetration depth λ and the Ginzburg–Landau coherence length ξ_{GL}.

it is given by

$$\lambda = \sqrt{\frac{m}{4\mu_o e^2 \psi_o^2}} , \tag{6}$$

where ψ_o is the equilibrium value of the order parameter in the absence of an electromagnetic field. The penetration depth sets the length scale according to which an external magnetic field decays exponentially inside the superconductor.

Finally, Ginzburg and Landau defined another parameter, the Ginzburg–Landau parameter $\kappa = \lambda/\xi_{GL}$, which plays an important role in the classification of superconductors with respect to their behavior in an applied magnetic field.

4.3 Type-I and type-II superconductors

The behavior of a superconductor in a magnetic field depends on two energy contributions: (i) the energy E_B that is necessary to expel the magnetic field from the superconductor and (ii) the energy E_C that is gained by the condensation of the Cooper pairs. Inside the superconductor both energies compensate each other, i.e., $-E_B = E_C = B_{c,th}^2/2\mu_o$ with the thermodynamic critical field $B_{c,th}$. However, at a S/N interface (superconductor to normal conductor interface) both energies are modified (see Figure 4), the magnetic field is not completely expelled and the Cooper-pair density is reduced. Therefore, the modification of these energies at a S/N interface with an area A is given by $\Delta E_B = A\lambda B_{c,th}^2/2\mu_o$ and $\Delta E_C = A\xi_{GL} B_{c,th}^2/2\mu_o$, respectively. As a consequence we obtain an energy contribution of a S/N interface of

$$\Delta E_C - \Delta E_B = (\xi_{GL} - \lambda)\, A B_{c,th}^2/2\mu_o , \tag{7}$$

which is positive for $\xi_{GL} > \lambda$ or negative for $\xi_{GL} < \lambda$. These different possibilities automatically give rise to different behaviors of the superconductor in an applied field. In one case S/N interfaces are energetically favored, in the other case not.

Exact calculations by Abrikosov in 1957 [12] predicted this behavior. He classified two types of superconductors according to their Ginzburg–Landau parameter. These superconductors are:

– *Type-I for $\kappa < 1/\sqrt{2}$*: Because of the positive energy necessary for the formation of S/N interfaces, these superconductors expel an applied magnetic field (except for

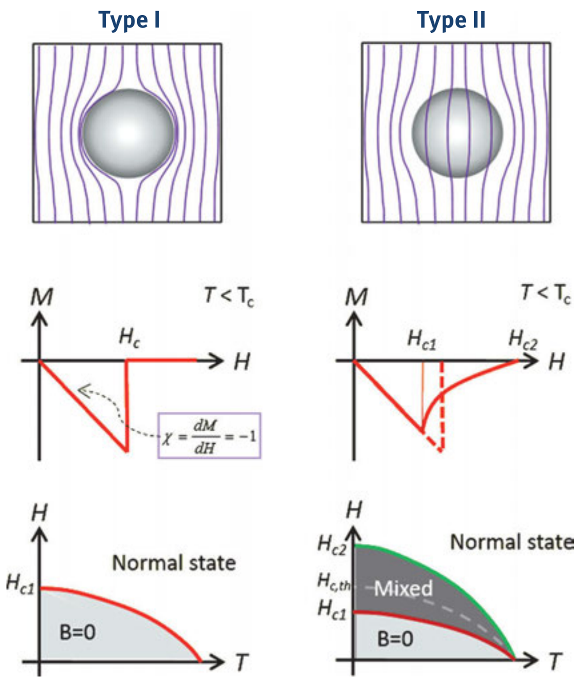

Fig. 5: Schematic sketches of the behavior of type-I and type-II superconductors in an applied magnetic field (top), magnetization in the superconducting state below T_c starting with ideal diamagnetism (Meissner phase with the magnetic susceptibility $\chi = -1$) followed by different types of field penetration (middle), and the resulting phase diagram with the Meissner state ($B = 0$), mixed state, and normal state separated by the different critical fields (bottom).

a thin layer at the surface) up to the critical field $H_c = H_{c,th}$. This is the Meissner–Ochsenfeld effect.

– *Type-II for* $\kappa > 1/\sqrt{2}$: These superconductors show a more complex behavior in an applied magnetic field. Only up to a first critical field H_{c1} is magnetic flux expelled. Above H_{c1} flux penetrates the superconductor since the formation of S/N interfaces are energetically favored. This phase is called the *mixed state* or *Shubnikov phase*. Nevertheless, superconductivity persists up to an upper critical field H_{c2}.

These different behaviors are shown in Figure 5.

In type-I superconductors the Meissner–Ochsenfeld effect takes place for fields below the critical field H_c. Above H_c the material becomes normal conducting (similar to the transition at T_c) and the magnetic field completely penetrates the superconductor, i.e., $M = 0$.

In contrast, type-II superconductors show a quite different behavior in a magnetic field:

(i) The Meissner–Ochsenfeld effect ($B = 0$) is only present below the lower critical field H_{c1}.
(ii) For higher fields, flux starts to penetrate the superconductor. However, superconductivity persists up the upper critical field H_{c2} and the magnetization is still finite ($M < 0$). The upper critical field is typically much larger than the critical field H_c or $H_{c,th}$ (see Table 1). This is one of the reasons why type-II superconductors are more suitable for technical applications.
(iii) Moreover, since $(\Delta E_C - \Delta E_B) < 0$ the superconductor tries to form as many N/S surfaces as possible. Therefore, the flux penetrates in the form of magnetic *flux lines* that contain the smallest possible amount of magnetic flux, the magnetic flux quantum $\Phi_o = h/2e = 2.07 \cdot 10^{-15}$ Wb. These flux lines (or fluxons) are quantum mechanical objects. They possess a normal conducting core of the size $2\xi_{GL}$, the magnetic field penetrating this normal core is surrounded by a superconducting current (see Figure 6). Because of this screening current these objects are also called vortices or *Abrikosov vortices*, taking into account their discoverer Abrikosov [12].
(iv) Finally, the arrangement, shape, mobility, and motion of these vortices are all easily affected by a large number of interactions and energies. The major contributions to be considered are:
   a. *Vortices-vortex interaction*: This interaction is repulsive. This can easily be understood by considering the interaction of the screening current of a vortex with the magnetic field of adjacent vortices. Already in 1957 Abrikosov predicted that the flux-lines would form a regular lattice. In an isotropic superconductor, this would be the closest 2D packing, i.e., a hexagonal or triangular lattice [12].
   The first experimental proof of a periodic structure of the magnetic field in the mixed phase was obtained in 1964 using neutron diffraction which demonstrated the basic periodic structure of the magnetic field [13]. Real images of the *Abrikosov vortex lattice* were first observed in 1966 by Essmann and Trauble using a magnetic decoration technique [14].
   However, small deviations and inhomogeneities, like anisotropic structural or superconducting properties or geometrical restrictions of the superconductor, can easily modify the structure of the (hexagonal) vortex lattice.
   b. *Driving forces*: There are a number of forces and energies that can act as a driving force for the motion of vortices in a superconductor. Major candidates are the *Lorentz force* $\boldsymbol{F}_L = \boldsymbol{J} \times \Phi_o$ caused by any applied current, thermal energy, and gradients in temperature or magnetic field. The motion of vortices causes dissipation in the superconductor.
   c. *Pinning force:* Fortunately, vortices can be ‘immobilized’ at defects in the material. This is called flux pinning or pinning.

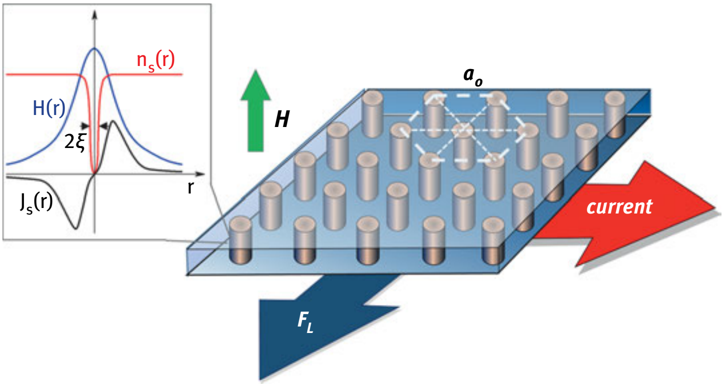

Fig. 6: Sketches of (left) a flux line with the radial distribution of the magnetic field H, the Cooper pair density n_S, and the circulating supercurrent J_S, and (right) the hexagonal flux line lattice with lattice parameter a_o and arrows indicating the impact of an applied current on a flux line lattice leading to the Lorentz force F_L.

The complex interplay of the different interactions leads to the volume pinning force and, finally, to the critical current density that defines the dissipation-free current regime for type-II superconductors. Since its understanding, especially in the novel, highly complex superconductors as well as in nanostructured and artificially modified systems, represents a major topic of this book, we will briefly sketch the main aspects of this part of vortex matter.

4.4 Flux pinning and summation theory

In order to retain a dissipation-free DC current flow or reduce the voltage noise due to vortex motion, the flux lines have to be pinned by defects. The pinning force of the defects compensates the driving force up to a critical value. In the case of the Lorentz force F_L this defines the maximum dissipation-free current density, i.e., the critical current density J_c given by

$$\boldsymbol{F}_c = -\boldsymbol{F}_L = \boldsymbol{B} \times \boldsymbol{J}_c \,, \tag{8}$$

where F_c represents the volume pinning force which is obtained via summation of the elementary pinning forces f_p [15]. The elementary pinning force describes the individual interaction between a single vortex and a single inhomogeneity or defect in the superconducting material. It arises from the local modification of the superconductor by the defect that results in a local reduction of the energy associated with the vortex.

Possible defects can be classified according to their:

– *Elementary coupling mechanism*, such as *magnetic interaction* or *core interaction:* The magnetic interaction is essentially determined by the field gradient in the superconductor (i.e., the penetration length λ), whereas the core interaction

arises from the interaction of locally perturbed superconducting properties with the variation of the superconducting order parameter (i.e., the coherence length ξ). Since in technical type-II superconductors with large Ginzburg–Landau parameters κ the penetration length is much larger than the coherence length, core interactions are usually more effective pinning sides. There exist two predominant mechanisms of core pinning, which are δT_c and $\delta\kappa$ pinning. Whereas δT_c pinning is, for instance, caused by spatial variations in the Cooper-pair density, elasticity, or pairing interaction, $\delta\kappa$ pinning is predominantly caused by variations of the electronic mean free path.
- *Size* or *shape:* In order to contribute to the summation of individual pinning forces, the effective pinning site should be of the order of the local gradient. This implies that the pinning site should be smaller than ξ or λ for core pinning or magnetic interaction, respectively. Extended defects like surfaces, extended holes (e.g., so called antidots) or cones typically trap flux lines or even multiple flux quanta, i.e., quantized magnetic flux $\Phi = n\Phi_0$.
- *Origin*: Real superconductor materials always contain *natural defects* such as vacancies, precipitates, dislocation loops, stacking faults, or grain boundaries that contribute to the volume pinning. In most cases, several different types of natural pinning defects exist. However, one can also introduce *artificial pinning defects*. Typical candidates for thin film applications are irradiation defects or specially patterned defects like moats or channels [16] or small holes (so-called antidots) [17, 18]. Artificial pinning sites, their preparation and impact on various superconducting properties represents an important topic of this book (see Chapters 6 and 7).

As indicated above, the mechanism of flux pinning and, thus, the critical current density in real type-II superconductors is determined by (i) the *interaction between individual vortices* (VV interaction), (ii) the *interaction between individual pinning centers and vortices* f_p, (iii) the *driving force* (e.g., Lorentz force caused by an applied current, a field or temperature gradient or even a finite temperature), and (iv) the *homogeneity* of the superconducting material in terms of the amplitude and length scale of the variation of the superconducting properties. Therefore, a number of problems have to be solved in order to understand the range of effects caused by vortex motion in type-II superconductors [15]:
- First, the dominant class or classes of defects, which are responsible for the pinning, have to be determined and their elementary pinning forces f_p have to be computed.
- Second, the 'response' of the vortex lattice to the individual pin-vortex interactions has to be determined. For a small driving force (static vortex lattice) and small pinning forces, this can be for instance an elastic response described by the elastic matrix [19], plastic deformations, or instabilities [20]. The different mechanisms are comparable to the reaction of solids upon internal stresses. As long

as the strain is small the vortex lattice can reach its equilibrium position with respect to the pin distribution without plastic shear taking place in the lattice. In the case of larger strains plastic shear will create a significant number of defects in the vortex lattice. The deformation of the vortex lattice can be described by the displacement field. It can be two-dimensional (transversal displacement) [20] or three-dimensional [21].

- Third, the summation of the effects of many pins, usually at random position, leads to the prediction of the volume pinning force F_p that takes into account the elementary vortex interaction, the distribution and density of pinning sites, and the kind of deformation in the vortex lattice. Note that F_p is not automatically identical to the force $F_\mathrm{c} = J_\mathrm{c}B$, which is defined by the onset of vortex motion.
  The summation problem can be solved in some ideal or model systems. In the easiest case every pinning center is able to exert its maximum pinning force f_p on the vortex lattice, and the net volume pinning force F_p would be given by the direct summation, i.e., $F_\mathrm{c} = F_\mathrm{p} = \sum (f_\mathrm{p}/V)$. This case is usually only observed in systems where individual flux lines are trapped by pinning sites, which is for instance the case for extremely small fields or superconductors with artificial defects. In all other cases the evaluation of the volume pinning force is more complex and requires summation in the formalism of the collective pinning theory [22].
- Finally, it is the mechanism of flux motion that determines the onset of dissipation and, therefore, the technically relevant critical current density $\boldsymbol{J}_c \times \boldsymbol{B} = \boldsymbol{F}_c$ with $F_\mathrm{c} \le F_\mathrm{p}$, which is determined in the experiment. The volume critical force F_c can differ strongly from the volume pinning force F_p, which is evaluated for the case of elastic deformations. It depends upon (a) the relation between vortex-vortex and vortex-pin interactions and (b) the homogeneity of the superconductor on a length scale larger than the coherence length [23–26]. This automatically leads to two different mechanisms of vortex dynamics.
  Pin breaking: If the differences between depinning forces of neighboring vortices are small compared to the vortex-vortex interaction, the complete vortex lattice will be pinned or depinned. This situation is referred to as pin breaking. The volume pinning is given by the statistical summation of the elementary interactions in the correlation volume $V_\mathrm{c} = L_\mathrm{c} R_\mathrm{c}^2$ according to the collective pinning theory introduced by Larkin and Ovchinnikov [22]

$$F_\mathrm{c} = F_\mathrm{p} = \sqrt{\frac{n \cdot \left\langle f_\mathrm{p}^2 \right\rangle}{V_\mathrm{c}}} = \sqrt{\frac{W(0)}{V_\mathrm{c}}}\,, \tag{9}$$

  with n denoting the density of pinning sites, $W(0)$ representing the pinning parameter, and L_c and R_c the correlation lengths perpendicular and parallel to the magnetic field direction, respectively. The resulting field dependence is given in Figure 7. Up to a given field the elastic deformation of the vortex lattice is sustained and the field dependence of the volume pinning force is nicely described by the

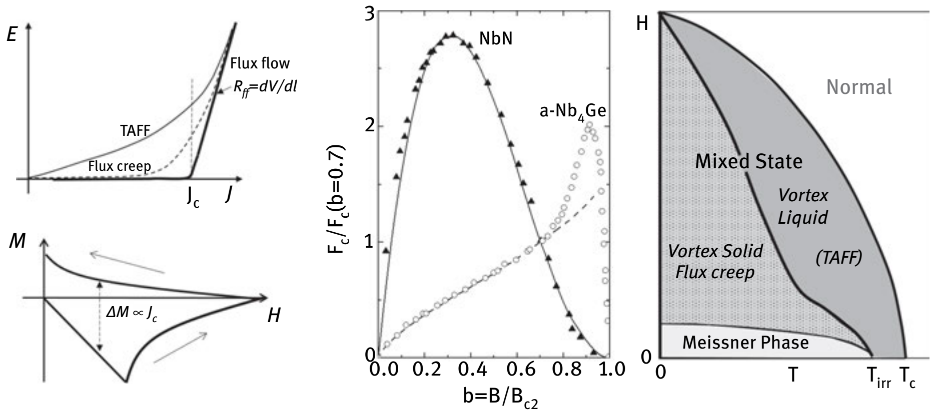

Fig. 7: The critical current is typically determined via resistive measurements (a) using a voltage criterion (typically 1 μV/cm) or magnetic measurements (b) for which the pinning manifests itself by a hysteretic behavior. According to the Bean critical state model the difference ΔM in the magnetic measurement is proportional to the critical current density [27]. The resulting field dependence of the normalized volume pinning force is shown in (c) for a weak pinning amorphous Nb_4Ge thin film ($F_P(b = 0.7)$ typically of the order of 10^5–10^6 N/m^3 at 2.2 K) [20] and a strong-pinning NbN thin film ($F_c(b = 0.7)$ typically of the order of 10^8–10^9 N/m^3 at 4.2 K) [24] demonstrating pin-breaking according to the 2D collective pinning theory (dashed line) and the flux line shear mechanism (solid line), respectively. Finally, tunneling and thermal activation leads to the phase diagram (d) with a Meissner state (no vortices), a vortex solid with flux creep, and a vortex liquid with thermally activated flux flow (TAFF). The latter regime is more prominent for high-T_c materials.

equation above. At high fields close to B_{c2}, plastic deformations in the flux-line lattice set in leading to an increase of the pinning force with respect to the predictions of the collective pinning theory. The so-called peak effect at high fields (see Figure 7) is a characteristic feature of the collective pinning behavior in weak pinning materials.

Flux-line shear mechanisms: When the local pinning force strongly varies over length scales comparable to or larger than the vortex-vortex distance, vortices or bunches of vortices will start to move independently as soon as the driving force exceeds the flow stress of the vortex lattice. In this so-called flux-line shear mechanism, F_c is determined by the vortex-vortex interaction, it is not given by the volume pinning force F_p of the weak or strong pinning areas, respectively. Generally F_c should range between these two quantities, i.e., $F_{p,\mathrm{strong}} > F_c > F_{p,\mathrm{weak}}$. As a result, the volume pinning force is determined by the plastic shear properties of the vortex lattice, since areas that are weakly pinned shear away from strongly pinned regimes. The resulting volume pinning force is given by [23–26]

$$F_c = G \cdot c_{66} \propto \frac{B_{c2}^2}{w} b\,(1-b)^2 \ , \tag{10}$$

with c_{66} representing the shear modulus of the vortex lattice, G a geometrical factor that accounts for the orientation of the flux-flow channels with respect to the driving force, and $b = B/B_{c2}$ the reduced applied magnetic field. The typical field dependence obtained for strong pinning superconductors is shown in Figure 7. It is characterized by a broad peak at low field around $B \approx B_{c2}/3$. The flux-line shear mechanism is usually encountered in strong-pinning systems, whereas only weak-pinning superconductors show collective pinning behavior.

The field dependencies for pin breaking and flux-line shear given in Equations (9)–(10) and in Figure 7 refer to the ideal case of very homogeneous systems and low temperatures. Samples with a distribution of pinning properties or superconducting properties show deviations from these ideal behaviors. Moreover, up to now we did not take into account the impact of other energies on the vortex motion. Especially for the high-T_c superconductors the impact of thermal energy has to be considered.

4.5 Flux creep and thermally assisted flux low

Although it was already discussed before, with the discovery of superconductivity it became evident that vortex motion for current densities $J < J_c = F_c/B$ has to be considered. Invoking a washboard-like pinning potential, individual vortices can tunnel (even at $T = 0$) or hop (e.g., thermally activated) from one potential well to the next one. This leads to two different behaviors which are, for instance, visible in the current-voltage characteristic (Figure 7a) and the phase diagram (Figure 7d).

Flux Creep: Tunneling of vortices was already predicted in 1962 and described later in the Kim-Anderson model for flux creep [30]. In this model, the tunneling rate of vortices is given by $R = \nu_0 \exp(-U/kT)$ where ν_0 is the attempt frequency (10^{-8}–$10^{-11}\,\mathrm{s}^{-1}$) and U the effective pinning potential (typically 10–1000 K). As a consequence an electric field is present already for $J < J_c$:

$$E = Bl\nu_0 \exp\left(-\frac{U}{kT}\left(1 - \frac{J}{J_c}\right)\right) , \tag{11}$$

with l representing the average hopping distance. The resulting current-voltage characteristic shows a shallow increase of the electric field below J_c (Figure 7a), the technically relevant critical current is therefore smaller than J_c. Nevertheless, the flux creep regime in the mixed state represents a vortex solid state (Figure 7d).

Thermally Assisted Flux Flow: At elevated temperatures the impact of the thermal energy kT cannot be neglected. As a result, vortices cannot only tunnel, they can also hop from one well in the pinning potential to the next one. This hopping can occur in or even against the direction of the Lorentzian force. The resulting electric field is larger than the field generated by the tunneling of vortices, it is described in the so-called thermally assisted flux flow model (TAFF) by [31]

$$
\begin{aligned}
E &= 2Blv_0 \exp\left(-\frac{U}{kT}\right) \sinh\left(\left(\frac{U}{kT}\right)\left(1-\frac{J}{J_c}\right)\right) \text{ , and} \\
E\,(J \to 0) &= J \cdot \left(2Blv_0 \frac{U}{J_c kT}\right) \equiv J \cdot \rho_{\mathrm{TAFF}} \text{ .}
\end{aligned}
\tag{12}
$$

As a result, flux motion leads to dissipation starting at zero current (Figure 7a) in the 'TAFF' regime of the mixed state, which therefore is called a vortex liquid state (Figure 7d). The vortex liquid state is separated from the vortex solid state by the so-called irreversibility line.

4.6 Josephson effects

Finally, we introduce one of the most intriguing effects in superconductivity, the *Josephson effects* named after their discoverer [32]. They are not only ideal manifestations of the macroscopic quantum-phenomenon of superconductivity, they also provide the basis for extremely sensitive devices that have revolutionized electromagnetic measurements. In general, the behavior of a tunneling junction (NIN, NIS, or SIS with N, I, and S denoting a normal metal, insulator, and superconductor, respectively) represent quantum-mechanical objects. Depending on the charge carriers, two different tunnel processes can be distinguished:

(i) Tunneling of so-called quasiparticles (electrons or holes) was discovered by Giaever in 1960 [33]. In the case of superconductor tunnel junctions (SIS or NIS), the quasiparticle tunneling represents an ideal tool to determine the energy gap (see Figure 8, and Chapter 1).
(ii) For the case of SIS junctions, additionally Cooper pairs can tunnel from one superconductor to the other. In contrast to the quasiparticle tunneling, where the tunneling is driven by a voltage difference between both conductors, the Cooper-pair tunneling is driven by the phase difference between the two superconductors. Since the phase difference can be constant (e.g., due to an applied magnetic field) or varying in time (due to a voltage difference between the superconductors) there exist two different effects, i.e., the DC Josephson effect and the AC Josephson effect, respectively [32].

Since the Josephson effects describe the behavior of superconductor tunnel junctions, we will briefly sketch the physics of tunneling in general before introducing the special effect of the tunneling of Cooper pairs.

4.6.1 Quasiparticle Tunneling

Tunneling through a barrier is only possible for quantum-mechanical particles, i.e., light particles like electrons. It can be described by the Schrödinger equation using the appropriate boundary conditions.

NIN tunnel junction: In NIN junctions, the tunneling current of the charge carriers (fermions) at a given voltage V and temperature is simply proportional to the tunneling probability T_n, the number of occupied states $D(E) \cdot f(E)$ of the normal conductor N_1, and the number of unoccupied states $D(E + eV) \cdot (1 - f(E + eV))$ of the second normal conductor N_2, into which the charge carriers tunnel. Here D and f represent the density of states and the Fermi–Dirac distribution, respectively. Via integration over the complete energy range and considering tunneling events in both directions, we obtain the resulting total tunneling current

$$\begin{aligned} I_{N_1IN_2} &= \frac{2\pi e}{\hbar}|T_n|^2 \int_{-\infty}^{\infty} D_{N_1}(E)\, D_{N_2}(E + eV)\,(f(E) - f(E + eV))\,\mathrm{d}E \\ &\approx \frac{2\pi e}{\hbar}|T_n|^2 D_{N_1}(E_F)\, D_{N_2}(E_F)\, eV \equiv G_{N_1IN_2} V \equiv \frac{1}{R_{N_1IN_2}} V\,. \end{aligned} \tag{13}$$

For the NIN junction the resulting current-voltage characteristic is simply ohmic (Figure 8a), i.e., $I \propto V$ with a proportionality factor given by the conductance G_{NIN} or the inverse resistance $1/R_{NIN}$.

NIS tunnel junction: Because of the energy gap 2Δ of the superconductor, the case of the NIS junction is a bit more complex (Figure 8b). Around the energy gap, the density of states of the normal charge carriers (fermions which due to their particle-like behavior are called quasiparticles) in a superconductor is given by:

$$\begin{aligned} D_S(E) &= D_N(E_F)\,\frac{E}{\sqrt{E^2 - \Delta^2}} \quad &\text{for} \quad |E| \geq \Delta \\ &= 0 \quad &\text{for} \quad |E| < \Delta\,, \end{aligned} \tag{14}$$

with $E_F := 0$. In analogy to the NIN junction the NIS tunnel current is given by:

$$\begin{aligned} I_{NIS} &= \frac{2\pi e}{\hbar}|T_n|^2 \int_{-\infty;\ \text{for } |E|>\Delta}^{+\infty} D_N(E)\, D_S(E + eV)\,(f(E) - f(E + eV))\,\mathrm{d}E \\ &\approx \frac{G_{NIN}}{e} \int_{-\infty}^{\infty} \frac{|E|}{\sqrt{|E^2 - \Delta^2|}}\,(f(E) - f(E + eV))\,\mathrm{d}E\,. \end{aligned} \tag{15}$$

For zero temperature and assuming a constant (i.e., energy independent) density of states around the Fermi level, this simplifies to:

$$\begin{aligned} I_{NIS} &= 0 \quad &\text{for} \quad |eV| < \Delta \ll E_F \\ &= \frac{G_{NIN}}{e}\sqrt{|(eV)^2 - \Delta^2|} \quad &\text{for} \quad |eV| \geq \Delta \ll E_F\,. \end{aligned} \tag{16}$$

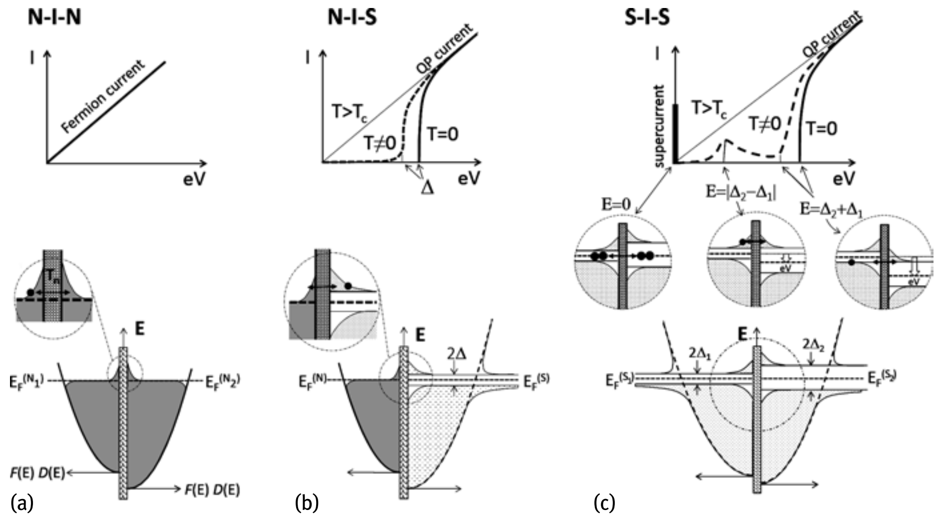

Fig. 8: Schematic diagrams of the current voltage characteristic (top) and density of states at the Fermi level (bottom) of a NIN (a), NIS (b), SIS (c) junction showing the tunneling events of the different contributions of the Fermi current (NIN), quasiparticles (NIS and SIS), and Cooper pairs (SIS). The insets show close-ups of the different tunnel events.

The resulting current voltage characteristics are shown in Figure 8b. For zero temperature, the onset of current occurs at $eV = \Delta(T = 0)$, at higher voltages the characteristic asymptotically approaches a linear behavior defined by the conductivity G_{NIN}. With increasing temperature the energy gap decreases (see also Figure 3a) and thermal activation leads to tunneling of the quasiparticles also for voltages $eV < \Delta(T)$. As a result the characteristics recorded at finite temperature are smeared out as indicated in Figure 8b. Nevertheless, the highly nonlinear behavior allows one to determine the energy gap $\Delta(T)$ as discussed in Chapter 1.

SIS tunnel junction: In principle, the SIS junction can be treated in an analogous way. The quasiparticle tunneling is given by:

$$\begin{aligned} I_{S_1 I S_2} &= \frac{2\pi e}{\hbar} |T_n|^2 \int\limits_{-\infty; for|E|>\max\{\Delta_1,\Delta_2\}}^{+\infty} D_{S_1}(E)\, D_{S_2}(E + eV)\, (f(E) - f(E + eV))\, \mathrm{d}E \\ &\approx \frac{G_{\mathrm{N_1IN_2}}}{e} \int\limits_{-\infty}^{\infty} \frac{|E|}{\sqrt{|E^2 - \Delta_1^2|}} \frac{|E|}{\sqrt{|(E + eV)^2 - \Delta_2^2|}} (f(E) - f(E + eV))\, \mathrm{d}E\,. \end{aligned} \tag{17}$$

However, the evaluation is quite complex, even for $T = 0$ K. Nevertheless, the current voltage characteristic can be obtained by considering a simple graphical representation of the density of states as sketched in Figure 8c.

4.6.2 Cooper Pair Tunneling

Up to now, we only considered the tunneling of the quasiparticles. However, already in 1962 Josephson predicted [32] that (i) Cooper pairs might also participate in the tunneling process and (ii) that due to the macroscopic quantum state of the superconductor this might result in some spectacular effects. Only one year later in 1963, the predictions were experimentally verified [34].

Since the tunneling of Cooper pairs is driven by the phase difference between the two superconductors and not by a voltage difference as in the case of quasiparticle tunneling, it is already present for $V = 0$. In general, Cooper pairs in a superconductor are quantum mechanical objects. They can be described by the time-dependent Schrödinger equation $i\hbar\partial\Psi/\partial t = E\Psi$ with the wave function $\Psi = |\Psi|e^{i\phi}$, the phase φ, and the superconducting condensate density $n_s = |\Psi|^2$. With a tunneling frequency T of the Cooper pairs, an applied voltage V between the two superconductors S_1 and S_2, the charge of the Cooper pairs $q = 2e$, and a definition of the zero-energy reference $E_\mathrm{F} := 0$, the basic set of equations which describe the tunneling of the Cooper pairs is given by

$$\begin{aligned} i\hbar\frac{\partial\Psi_1}{\partial t} &= \hbar T\Psi_2 - eV\Psi_1 \\ i\hbar\frac{\partial\Psi_2}{\partial t} &= \hbar T\Psi_1 + eV\Psi_2 \,. \end{aligned} \tag{18}$$

Equation (18) shows that the condensate density $n_\mathrm{s} = |\Psi|^2$ in S_1 is increased by the tunneling of Cooper pairs from S_2, and vice-versa. Furthermore, the difference in energy between S_1 and S_2 is given by $(2e)V$, which for mathematical reasons is symmetrized over the two superconductors. Assuming identical superconductors (i.e., $n_\mathrm{s} \approx n_\mathrm{s}(S_1) \approx n_\mathrm{s}(S_2)$), Equation (18) leads to expressions for the phase difference between the two superconductors and the superconducting tunneling current J

$$\frac{\partial\left(\phi_2 - \phi_1\right)}{\partial t} = -\frac{2e}{\hbar}V \quad \text{or:} \quad \Delta\phi = \phi_2 - \phi_1 = -\frac{2e}{\hbar}Vt + \text{const.}\,, \tag{19}$$

with $2\,\mathrm{eV}/\hbar = \omega$ representing an angular frequency, and

$$J\left(t\right) = \frac{\partial n_s\left(S_1\right)}{\partial t} = -\frac{\partial n_s\left(S_2\right)}{\partial t} = Tn_s \sin\left(\Delta\phi\right) = J_0 \sin\left(\gamma_0 - \omega t\right) \,. \tag{20}$$

These two expressions automatically lead to the two different Josephson effects.

DC Josephson effect: For zero-voltage, the tunneling current is simply determined by the phase difference between the two superconductors:

$$J = J_0 \sin\left(\Delta\phi\right) \,. \tag{21}$$

Since $V = 0$, this phase difference is constant in time. However, it can be modified by an applied magnetic flux in the junction. As a result, the tunneling current varies in a sinusoidal way upon the applied magnetic field. This effect is, for instance, used in extremely sensitive magnetic field sensors, superconducting quantum interference devices (SQUID). A detailed report on recent developments on NanoSQUIDs is given in Chapter 11.

AC Josephson effect: For voltages $V \neq 0$, the phase varies in time and we automatically obtain an AC tunneling current with a voltage-dependent frequency:

$$f_J = \frac{2e}{h} V \,. \tag{22}$$

The maximum voltage that can be applied to the tunnel junction is given by $V_{max} = \Delta/(2e)$. Therefore, the maximum frequency that can be generated by the Josephson junctions is $f_{J,max} = \Delta/h$. For Al, Nb, and BSCCO, with gaps of 0.17 meV, 1.45 meV, and ~ 25 meV (see Table 1), the maximum frequencies are 82 GHz, 700 GHz, and 12 THz, respectively. This demonstrates that the AC Josephson effect represents a relatively easy way to generate or detect GHz and even THz frequencies. In the latter case, an AC signal would directly be converted to a voltage signal.

This principle became even more attractive with the discovery of the intrinsic Josephson effect in the highly anisotropic high-T_c superconductors in 1992 [35]. Because of the high anisotropy and short coherence length compared to the lattice spacing between the superconducting CuO planes in $Bi_2Sr_2CaCu_2O_8$, the 2D superconducting layers are seemingly intrinsically separated by an ‘insulating layer’. In this way they form stacks of natural (i.e., intrinsic) SIS junctions. In the meantime, the intrinsic Josephson effect has been observed in a number of other systems. Since these SIS stacks form naturally and since the AC Josephson current density is potentially very high, these systems are very promising candidates for various GHz to THz applications. Recent developments in this field are reviewed in Chapter 12.

5 Application of superconductivity

In the previous sections, we introduced the basic aspects of the quantum mechanical phenomenon called superconductivity. We demonstrated that the macroscopic quantum state of the Cooper pairs results in:

(i) *perfect conductivity* resulting in zero-resistance $\rho = 0$ at dc current and a very small microwave surface resistance at high frequencies;
(ii) *perfect diamagnetism* (Meissner–Ochsenfeld effect);
(iii) *quantization of magnetic flux* resulting in the formation of single-quanta (or multiquanta) vortices that interact with each other and with defects in the superconductor, and;
(iv) *phase correlation* of the charge-carrier wave function which in weak-link structures leads to the Josephson effects.

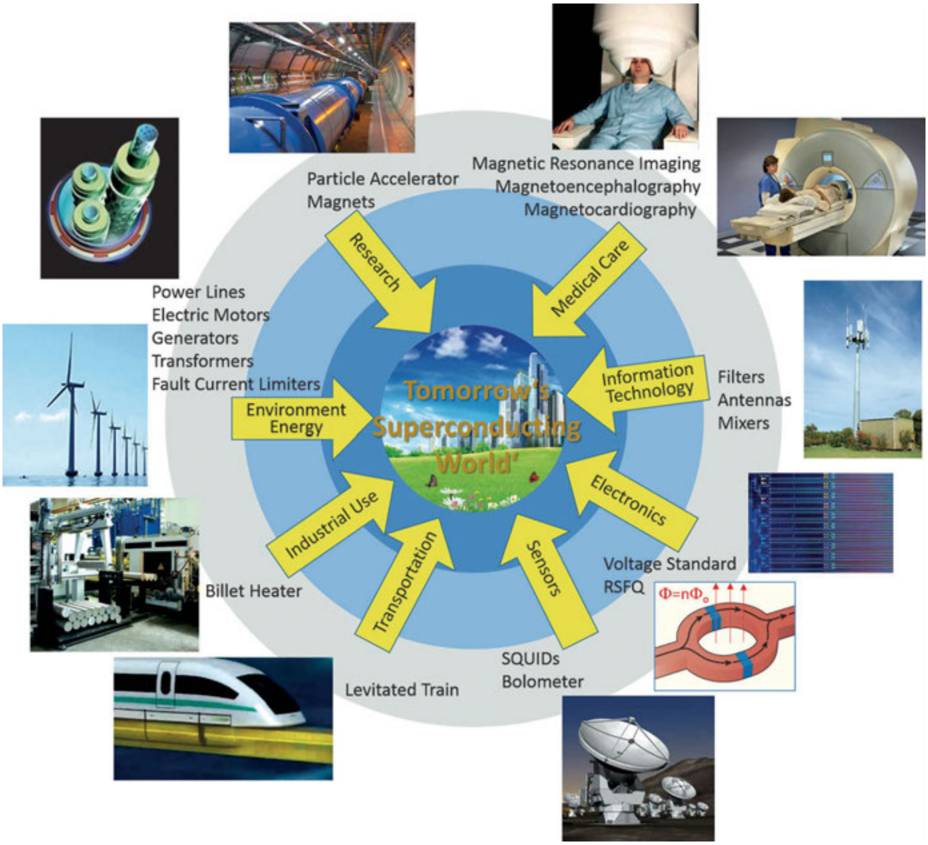

Fig. 9: 'Tomorrows Superconducting World' shows where we already benefit from superconductivity or could benefit from it in the future.

These extraordinary properties mean that superconductivity offers a high potential for improvement of existing applications or even novel applications in various fields. Existing, relatively well-established applications are (Figure 9):

- Medical care: A number of diagnostic superconductor applications are well established in medical care. Magnetic resonance imaging (MRI) is widely used for visualizing organs and structures inside the human body. Similarly, magnetoencephalography (MEG) is used for analysis of the brain and brain activities. Other applications are feasible, e.g., magnetocardiography (MCG) measuring the magnetic activity of the heart could become the counterpart to electrocardiography (ECG).
- Information technology, electronics, and sensors: Superconductivity bears the potential to improve quite a number of technologies. For instance, superconducting filters, antennas, and mixers can improve the performance of the data

transmission and data handling of base stations for cell phones. Even complex ultrafast electronics, the so-called 'software radio' is being considered for the improvement of data handling in devices like base stations.
The extreme magnetic field sensitivity of the so-called Superconducting Quantum Interference Device (SQUIDs) is used for various kinds of highly sensitive sensors (e.g., magnetometers, amplifiers, current meters, and particle detectors). Superconducting bolometers are well established in radio astronomy. They could also become attractive for other bolometric applications.
Finally, complex circuits based on Josephson arrays could be used for various electronic applications ranging from standards (e.g., voltage standards) and logic devices, to quantum computing (e.g., Rapid Single Flux Quantum Logic, RSFQ).
– Environment, energy, industrial use, and transportation: The majority of applications in this field is based on the use of superconducting cables. On the one hand, superconducting cables can be used in power lines leading to a significant reduction of the losses. On the other hand, wound into coils they can be used in high-field magnets or electric motors and generators. The superconducting billet heater represents an example for the use of superconducting magnets for industrial application. Superconducting motors or generators benefit from their large power density, which could be used to enhance the power or reduce the volume and mass of the device. This would be very attractive for larger engines or generators, like ship's engines, hydro or wind turbines.
– Research: Last but not least, superconductor applications are well established in various fields of contemporary research. Outstanding examples are particle accelerators and fusion reactors. However, high-field magnets, imaging technologies (e.g., nuclear resonance imaging), or superconducting sensors (e.g., SQUIDs or bolometers) are also successfully used in many laboratories.

6 Superconductors at the nanoscale

The list above (see also Figure 9) demonstrates that there are quite a number of well-established applications of superconductivity. However, there are even more less-established or potential applications that either benefit from the use of superconductivity or are only feasible due to superconductivity. In order to develop the full potential of superconductors, it is essential to analyze, understand, engineer, and optimize them at the nanoscale. There are a number of very important questions and problems that are worth examining in this context (see also Figure 10):
– Improvement of superconductors, critical parameters: The critical parameters T_c, B_{c2}, and J_c define the operating regime. The enhancement of these critical parameters is one aim of superconductor research. The search for systems with higher transition temperatures, if possible even 'room temperature superconduc-

tivity', is definitely the research that attracts the most publicity. Nevertheless, it depends on the kind of application and which of the critical parameters represents a restriction and should be increased (typically, J_c and B_{c2} for high-field applications, J_c for low-field applications). Whereas T_c and B_{c2} represent material-specific parameters, J_c depends on the defects (type, density, arrangement) in the superconductor. Thus, in the first case, research on new superconductors is required. In the latter case, the role of pinning sites (i.e., type of defect, defect density and distribution) has to be analyzed, understood, and optimized. The introduction of pinning sites can be affected by the preparation process of the superconductor. However, they can also be introduced artificially after or during growth. In both cases this requires manipulation of the material on the scale of the coherence length, i.e., at the nanoscale.

– Vortex matter and fluxonics: The vortices and vortex lattice are not only quantum mechanical objects, they are also ideal nano-objects. Vortices possess a normal core of $\sim 2\xi$. As indicated above, pinning sites of nanometer size are required for optimized pinning of these vortices. However, the lattice parameter is also of nanometer size. Moreover, it can be varied over a large range by varying the applied field. An undistorted hexagonal vortex lattice has a lattice parameter $a_0 = 1.15(\Phi_0/B)^{1/2}$, i.e., a_0 varies from 166 nm to 53 nm to 17 nm for 100 mT, 1 T, and 10 T, respectively. Regular arrays of pinning sites (natural or artificial) can be used to achieve commensurability or matching between the vortex lattice and the pinning array. Moreover, subtle arrangements of pinning defects can be used for novel fluxonic concepts (e.g., flux guidance, vortex ratchets, vortex transistors) or improvement of existing device concepts (e.g., noise reduction in SQUIDs, frequency tuning of filters and antennae).
– Josephson physics: The second obvious nano-objects are tunnel junctions leading to the Josephson effects. The fabrication of the nanosized barrier between the two superconductors is highly demanding, especially if several (two junctions per dc SQUID, thousands for complex electronic circuits like voltage standards or RSFQ) identical tunnel junctions are required. Moreover, due to the miniaturization of electronics and sensors the fabrication of the individual device components require a reliable and reproducible preparation at the nanoscale.
– Anisotropy, 2D structure of high-T_c materials: Most applications still operate at 4 K, which requires liquid-He cooling or quite expensive cryocooling. The discovery of the high-T_c superconductors opened the temperature window for less-expensive operation using liquid nitrogen at 77 K or simpler cryocoolers. However, the enhancement of T_c has been achieved by a higher complexity of the superconductor, a 2D layered structure, and an extremely small coherence length (e.g., $YBa_2Cu_3O_7$ with $\xi_{ab} \approx 1.6$ nm and $\xi_c \approx 0.3$). Thus, the 2D nature and the small coherence length generally require additional engineering of these complex materials at the nanoscale.

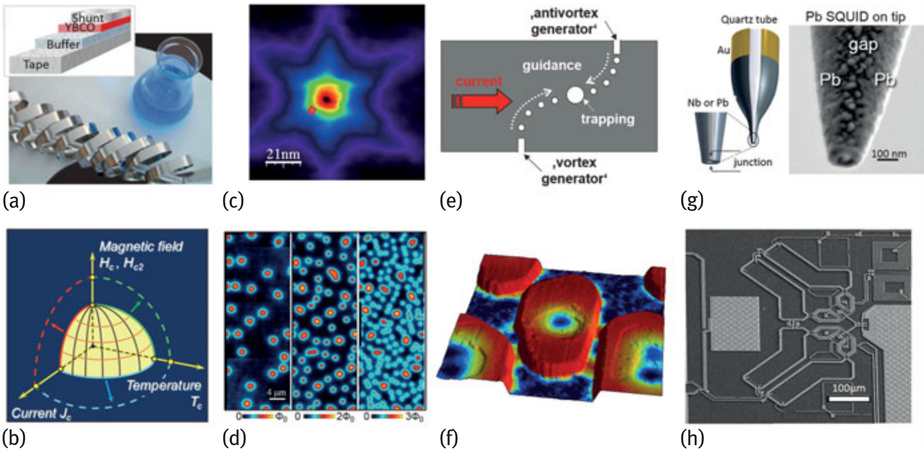

Fig. 10: Some of the strategies in the research on '*Superconductors at the Nanoscale*' that are discussed in this book. (a) Chemical deposition of high-T_c films as an example for the development of improved or novel preparation technologies, for instance, for HTS coated conductors (see Chapter 6), (b) improvement of critical properties of existing superconductors and search and understanding of novel superconductors, (c) analysis and visualization of nanophysics in superconductors (here: microscopy on a single vortex) (see Chapter 1), (d) analysis of interactions and collective phenomena on the nanoscale, (here: coexistence of single and multiquanta vortices) (see Chapters 4 and 5), (e) development of novel concepts to manipulate superconducting properties at the nanoscale (here: fluxonic concept for vortex manipulation via nanoscale patterning) (see Chapter 7), (f) examination of the physics in superconductors at extremely small scales (here: granularity, superconductivity, Josephson behavior in nanosize superconducting islands) (see Chapter 3), (g) novel nanosize applications (here: NanoSQUID on a tip) (see Chapters 9–15), and (h) complex devices composed of nanosize components (here: SQUID-based microsusceptometer) (see Chapters 11–15).

– Combination of superconductors and nonsuperconductors: In the end, the superconductor has to be connected to the 'outer world', i.e., to nonsuperconducting materials. Moreover, the combination with nonsuperconducting material might provide novel and interesting properties. This is, for instance, the case for superconductor-ferromagnetic hybrid systems. In all cases, the small superconductor coherence length requires an understanding and optimization of the interface between the superconductor and the nonsuperconductor at the nanometer scale.

It is the aim of this book to provide an overview of the state of research and novel approaches for the questions and problems that are addressed above. It comprises an up-to-date view on the research and a contemporary perspective on '*Superconductors at the Nanoscale*'.

Bibliography

[1] Kamerlingh-Onnes H. Proc. R. Acad. Amsterdam 11:168, 1908.
[2] Kamerlingh-Onnes H. Commun. Leiden, Suppl. Nr. 34, 1913.
[3] Bednorz JG, Müller KA. Z. Phys. B 64:189, 1986.
[4] Wu MK, Ashburn JR, Torng CJ, Hor PH, Meng RL, Gao L, Huang ZJ, Chu CW. Phys. Rev. Lett. 58:908, 1987; Zhao ZX. Int. J. Mod. Phys. B 1:179, 1987.
[5] Nagamatsu J, Nakagawa N, Muranaka T, Zenitani Y, Akimitsu J. Nature 410:63, 2001.
[6] Takahashi H, Igawa K, Arii K, Kamihara Y, Hirano M, Hosono H. Nature 453:376, 2008.
[7] Bardeen J, Cooper LN, Schrieffer JR. Phys. Rev. 108:1175, 1957.
[8] Townsend P, Sutton J. “Investigation by Electron Tunneling of the Superconducting Energy Gaps in Nb, Ta, Sn and Pb,” Phys. Rev. 128(2):591–595, 1962.
[9] Tinkham M. Introduction to Superconductivity. Dover Publications, 1996, p. 63.
[10] Ginzburg VL, Landau LD. Zh. Eksp. Teor. Fiz. 20:1064, 1950. English translation in: Landau LD. Collected papers. Oxford: Pergamon Press, 1965, p. 546.
[11] Gor’kov LP. Sov. Phys. JETP 36:1364, 1959.
[12] Abrikosov AA. Zh. Eksp. Teor. Fiz. 32:1442, 1957 (English translation: Sov. Phys. JETP 5:1174, 1957]).
[13] Cribier D, Jacrot B, Madhav Rao L, Farnoux B. Phys. Lett. 9:106, 1964.
[14] Essmann U, Trauble H. Phys. Lett. A 24:526, 1967; J. Sci. Instrum. 43:344, 1966.
[15] Wördenweber R. Rep. Prog. Phys. 62:187–236, 1999.
[16] Pruymboom A, Kes PH, van der Drift E, Radelaar S. Phys. Rev. Lett. 60:1430, 1988.
[17] Baert M, Metlusko VV, Jonckheere R, Moshchalkov VV, Bruynseraede Y. Phys. Rev. Lett. 74:3269, 1995.
[18] Castellanos AM, Wördenweber R, Ockenfuss G, v.d. Hart A, Keck K. Appl. Phys. Lett. 71:962, 1997.
[19] Brandt EH. Phys. Stat. Sol. B 77:551, 1976; J. Low Temp. Phys. 26:709 and 735, 1977; J. Low Temp. Phys. 28:263 and 291, 1977.
[20] Wördenweber R, Kes PH, Tsuei CC. Phys. Rev. B 33:3172, 1986.
[21] Wördenweber R, Kes PH. Phys. Rev. B 34:494, 1986.
[22] Larkin AI, Ovchinnikov YuN. J. Low Temp. Phys. 34:409, 1979.
[23] Kramer EJ. J. Nucl. Mater. 72:5, 1978.
[24] Pruymboom A, Kes PH, van der Drift E, Radelaar S. Appl. Phys. Lett. 52:662, 1988.
[25] Welch DO. J. of Adv. Science 4:81, 1992.
[26] Wördenweber R. Phys. Rev. B 46:3076, 1992.
[27] Bean CP. Magnetization of high-field superconductors, Phys. Rev. Lett. 8:250, 1962; Rev. Mod. Phys. 36:31, 1964.
[28] Meissner W, Ochsenfeld R. Naturwissenschaften 21:787, 1933.
[29] London F, London H. Z. Phys. 96:359, 1935; London F. Une conception nouvelle de la supraconductivite, Hermann and Cie, Paris, 1937.
[30] Anderson PW. Phys. Rev. Lett. 9:309, 1962; Anderson PW, Kim YB. Rev. Mod. Phys. 36:39, 1994.
[31] Kes PH, Aarts J, van den Berg J, van der Beek CJ, Mydosh JA. Supercond. Sci. Technol. 1:242–248, 1989.
[32] Josephson BD. “Possible new effects in superconductive tunnelling,” Phys. Lett. 1:251, 1962; “The discovery of tunnelling supercurrents”. Rev. Mod. Phys. 46:251, 1974.
[33] Giaever I. “Energy Gap in Superconductors Measured by Electron Tunneling”, Phys. Rev. Lett. 5:147–148, 1960; Giaever I. “Electron Tunneling Between Two Superconductors”. Phys. Rev.

Lett. 5:464, 1960; Giaever I. “Electron tunneling and superconductivity”. Rev. of Modern Phys. 46:245, 1974.

[34] Rowell JM, Anderson PW, Thomas DE. Image of the Phonon Spectrum in the Tunneling Characteristic between Superconductors. In: Phys. Rev. Lett. 10:334, 1963.

[35] Kleiner R, Steinmeyer F, Kunkel G, Müller P. Intrinsic Josephson effects in Bi2Sr2CaCu2O8 single crystals, Phys. Rev. Lett. 68:2394, 1992.

Isabel Guillamón, Jose Gabriel Rodrigo, Sebastián Vieira, and Hermann Suderow

1 Imaging vortices in superconductors: from the atomic scale to macroscopic distances

Abstract: The Scanning Tunneling Microscope (STM) was used at cryogenic temperatures soon after its invention in the early 1980s. However, it has only been a few years since its full potential for studying superconductors has been developed. Here we provide an introduction to cryogenic STM applied to superconductors and the superconducting vortex lattice. We review STM basics, explaining how we measure the superconducting density of states by atomic-scale tunneling. We also discuss Andreev and Josephson features in tunneling conductance and the direct visualization of thermally induced vortex depinning, vortex motion and vortex melting. Finally, we discuss how to analyze large-scale vortex images, explaining calculations of angular and positional correlation functions and the displacement correlator, and show how these characterize the degree of disorder in the vortex lattice.

Keywords: Scanning probe microscopy, Tunneling spectroscopy, vortex physics, superconductivity.

1.1 Introduction

Tunneling spectroscopy is useful to the study of superconductors because it directly provides the superconducting density of states. In junctions formed by two superconductors, Tunneling spectroscopy also shows the coupling of the Cooper pair wavefunctions through the Josephson effect. During the 1960s and 1970s, many Tunneling spectroscopy experiments were performed. These used layers of an insulating material to form a tunnel barrier for electron transport between the two electrodes. The experiments were often quite conclusive, providing strong experimental support for the Bardeen Cooper and Schrieffer (BCS) theory through the measurement of the superconducting gap and of the electron-phonon pairing interaction in many different materials (see for example [1]).

The invention of the Scanning Tunneling Microscope (STM) by [2] opened the door to tunneling experiments at atomic level, having vacuum as the tunnel barrier. The superconducting tunneling conductance was first measured using an STM by [3] in the technologically important material Nb_3Sn. Subsequent tunneling conductance mea-

Isabel Guillamón, Jose Gabriel Rodrigo, Sebastián Vieira, Hermann Suderow, Laboratorio de Bajas Temperaturas y Altos Campos Magnéticos, Unidad Asociada UAM/CSIC, Departamento de Física de la Materia Condensada, Instituto de Ciencia de Materiales Nicolás Cabrera and Condensed Matter Physics Center (IFIMAC), Universidad Autónoma de Madrid, Spain

DOI 10.1515/9783110456806-002,

surements using STM were done in the cuprates by [4] and [5]. With an STM, one can also perform scanning tunneling spectroscopy and obtain maps of the tunneling conductance as a function of the position with atomic resolution. This makes the STM at low temperatures the only instrument able to map the superconducting density of states with a spatial resolution far below the superconducting coherence length ξ. The Abrikosov vortex lattice was first observed using an STM by [6], with a spatial resolution that exceeded considerably all other vortex visualization techniques.

The key constructive element of the STM is the piezoelectric ceramic, which literally plays the role of a finger touching the nanoworld. In fact, when the STM was invented, people immediately realized the potential of the idea behind it, developing a whole set of new methods to probe matter at the nanoscale by tracing other probes as a function of the position, as for example the force between a tip and the sample. Very soon after the invention of the STM, [7] developed the atomic force microscope, which is today widely used in physics, chemistry and biology. Different probes measuring magnetic fields at the surface were also developed, in particular with more recent advances in nanometric fabrication. Detailed images of vortex lattices have been obtained using magnetic force microscopy, scanning SQUID microscopy, and scanning Hall microscopy. These efforts are reviewed in [8, 9] and [10].

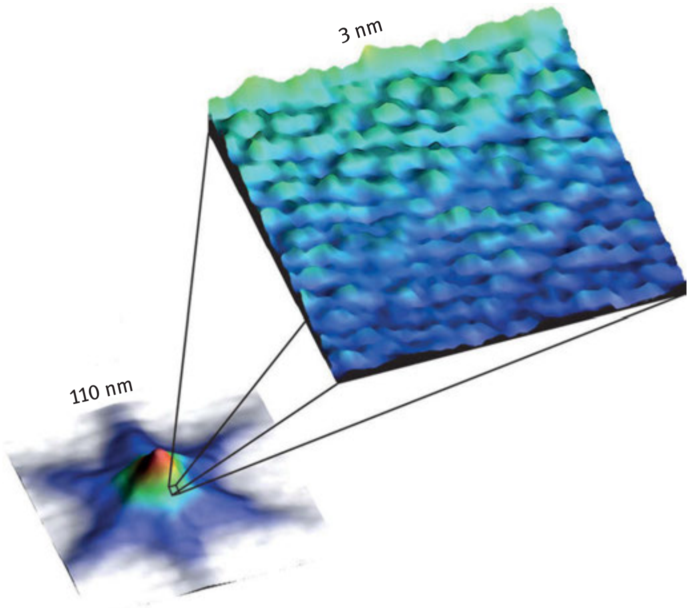

Fig. 1.1: Superconducting vortex in 2H-$NbSe_2$ imaged using STM at length scales of the order of several hundred nm (bottom) and at atomic scale (top). The figures show maps of the zero bias conductance acquired at 0.1 K and 0.03 T. There is a strong spatial variation of the superconducting density of states at all length scales, including at atomic distances. Figure adapted from Ref.[11].

As so often, opening a new window into smaller length scales provides information that could not have been anticipated previously. For example, the features in the superconducting density of states at length scales well below the superconducting coherence length ξ shown in Figure 1.1. This does not conform with the conventional view of superconductivity being homogeneous below ξ.

In this tutorial we explain the main concepts needed to design and understand this and other STM experiments in superconductors. We start by introducing the differences between macroscopic and atomic size tunneling and the role of the distance between tip and sample in normal and superconducting phases. We then discuss the results obtained from maps of the superconducting properties as a function of the position at different length scales, ranging from subnanometer to micrometer scales.

We focus mostly on work performed by our group. We also mention work by other groups whenever needed to explain concepts. But we do not aim at providing a complete reference list. For this, we refer to the reviews by [12, 13] and [14].

1.1.1 Formalisms to treat atomic size tunneling

One of the reasons for the success of STM is that the requirements to obtain atomic resolution on a surface are not as stringent as one may think a priori. One needs of course an atomically flat surface. But the tip can be totally blunt at nm length scales, mostly because the tunneling current depends exponentially as a function of the distance between both tunneling elements. Thus, the tunneling current decreases exponentially and only the outermost tip's atom provides a sizeable tunneling current.

Furthermore, the vacuum tunneling problem can be understood in simple terms for most purposes. Tunneling experiments are based on the quantum mechanical overlap between tip and sample's electronic wavefunctions, which is in general nearly impossible to calculate accurately. The nature of the tip's atom involved in tunneling is not known, it may be an atom of the tip's material (often Pt or Au) but it might well also be an atom picked up from the surface during the scanning process. Even less is known about what kind of electronic orbitals couple together. It turns out that, for most practical processes, the details of the quantum mechanical overlap between tip and sample's electronic wavefunctions do not matter. [15] found that the resulting tunneling current at zero bias voltage and zero temperature is simply proportional to the Fermi level local density of states of the sample at the position of the tip. They used a perturbative treatment of the tunneling current, valid when the overlap between wavefunctions is small, or, for practical purposes, when the tip is sufficiently far apart. Their treatment is based on Bardeen's transfer Hamiltonian formalism and requires knowing the shape of the tip and sample wavefunctions. [16] and [17] assume an s-wave tip wavefunction and find that the STM experiment provides a spatial map of the electronic density of states at an energy fixed by the bias voltage. The current versus bias voltage can be written as

$$I(V) \propto \int N_S(E) N_T(E - eV)\,(f(E) - f(E - eV))\,\mathrm{d}E \tag{1.1}$$

where $N_S(E)$ is the sample's density of states, $N_T(E)$ is the tip's density of states and $f(E)$ the Fermi function. The derivative of $I(V)$ is the convolution of $N_T(E)N_S(E)$ with the derivative of the Fermi function. The tunneling matrix elements are part of the proportionality factor. Their energy and spatial dependence are often neglected, although generally this is not true. The energy scale for the superconducting gap is typically far below the energy scales of localized states within the junction and of the energy range where the density of states of the tip $N_T(E)$ varies. Therefore, for most purposes, the tunneling conductance maps $N_S(E)$ of superconductors with enough accuracy at atomic scale.

1.1.2 Electronic scattering and Fermi wavelength

Most superconductors are good metals. Tunneling into an atomically flat metal can also be understood as tunneling into a Fermi sea of free electrons, or a Fermi liquid in the presence of interactions. Actually, this is a classical problem of STM. In practically all discussions about STM imaging, there is a dichotomy between tunneling into localized atomic orbitals and tunneling into the Fermi sea of free (or interacting) electrons. Both points of view lead to radically different images (Figure 1.2a,b and c). Tunneling into atomic orbitals provides the atomic positions at the surface. Tunneling into the Fermi sea, by contrast, provides flat images often with no atomic resolution. In exchange, disturbances to the Fermi sea in the form of defects, step edges or impurities appear as wave-like patterns, whose periodicity is given by the Fermi wavelength λ_F. The STM can be used to trace these patterns as a function of the energy and to measure the dispersion relation for occupied and empty electronic states.

An isolated charge in a free electron system is screened away by changes in the local electron density. This is described in the simplest way within the Thomas–Fermi approximation. Taking into account Bloch wavefunctions leads to Friedel oscillations, which quite often provide the actual answer of a free electron system to an impurity (see for example the book of [18]). Ideally, scanning over a free electron gas with a metallic tip provides flat and featureless images, because the electronic density of the sample is independent of the position. Close to a scattering center, such as an impurity or a step edge, Friedel oscillations produce variations in the local electronic density at the surface. These oscillations are detected in an STM and their energy dependence provides the corresponding dispersion relation. Surfaces of simple metals such as Au or Ag have been extensively studied for example by [19], [20] and [21]. Defects having a preferred orientation, such as step edges or structured impurities (e.g., dimers or chains), provide patterns with higher densities of states along certain directions. The

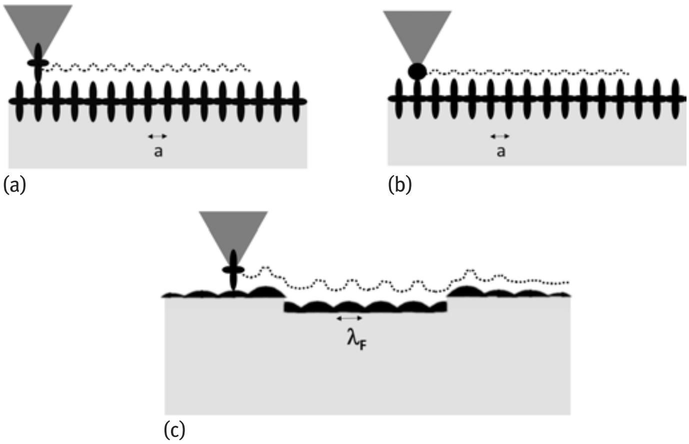

Fig. 1.2: In (a) and (b) we show a schematic view of different tip wavefunctions, eventually leading to different corrugations in the STM images. The sample is represented by the light gray rectangle and the outgoing atomic wavefunctions by the dark orbital-like features. The tip is represented by the dark gray triangle. The wavefunction of the atom at the tip apex is shown in black. The dashed line gives the signal sent to the feedback loop that maintains a constant current between tip and sample. The corresponding periodicity provides the atomic lattice. In (c) we schematically discuss the situation found in metals with strongly delocalized electron wavefunctions. The bulk electron wavefunctions are scattered at the surface at step edges, leading to oscillations in the density of states (dark structures on top of the sample's surface) with a wavelength of λ_F. Scanning the tip over the surface then provides periodic structures with wavelength λ_F.

energy dependence then gives the electronic dispersion relation along these directions only. If impurities or defects are point-like, the conductance images provide directly the reciprocal state shape of the electronic dispersion relation (see for example [22]).

In Figure 1.3a we present cartoon pictures of possible patterns observed at the surface. On the top left panel of Figure 1.3a we show a circular pattern created by a point-like impurity in a system with a circular Fermi surface. In the top right panel we show the pattern formed by a step edge located in the middle of the panel ($x = 0$) in a system with a spherical Fermi surface. In the bottom left panel we show patterns by two perpendicular step edges. In the bottom right panel we show the pattern obtained by a point-like impurity in a system with a square Fermi surface with sides along the x- and y-axis of the figure. In Figure 1.3b we represent the dispersion relation of a hole band. The energy dependence of the surface patterns for the case of a spherical Fermi surface are shown in the bottom panels in reciprocal space. There are circular features with higher intensity at the wavevectors given by the dispersion relation at $E = eV$, where e is the electron charge and V the applied bias voltage. The size of the k-space feature decreases with increasing energy in a hole band, and the opposite can be expected for an electron band.

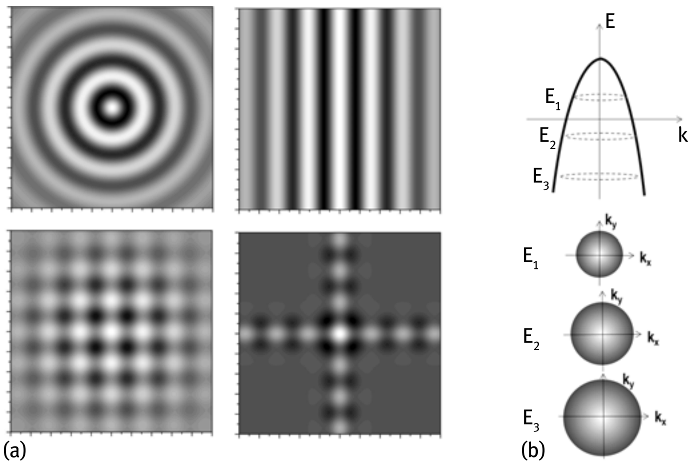

Fig. 1.3: In (a) we represent schematically the expected local density of states in real space at the surface of metals with a defect or impurity in 2D color maps. The value of the density of states is given by the color scale (white being the highest). We show four different cases in (a), a point-like impurity (upper left panel), a linear defect (upper right panel), two perpendicular linear defects (lower left panel) and a strongly anisotropic, square fold, Fermi surface (lower right panel). In (b) we represent (thicker line) schematically a dispersion relation in the top panel and the reciprocal space patterns expected for varying energies in the bottom panels.

The intensity of the observed modulations is given by the imaginary part of the Green function, which in turn includes the bare electron dispersion relation modified by correlations. Kinks in the band structure, van Hove singularities or places with strong electron-phonon scattering provide modified intensities at the relevant energies. This can be dramatic in some systems, such as the cuprate superconductors, where most of the scattering comes from a set of wavevectors connecting parts of the Fermi surface with an enhanced electronic density of states (see for example [23] or [12]), or in the pnictide superconductors, where the nematic electronic properties provide preferred scattering along certain directions (see for a review [13]). Conversely, knowing in advance the band structure and character of the impurity can be useful to locate an impurity embedded in the material, as shown by [24].

1.1.3 Tunneling with multiple conductance channels

A magnetic impurity embedded in a metal often produces a Kondo effect at low temperatures. The Kondo mechanism quenches the spin of the impurity by producing a singlet state with an electronic cloud surrounding the impurity (see for example the book of [18]). Therefore, tunneling into a Kondo impurity occurs in two channels in parallel, one into the free electron cloud and another one into the localized magnetic state of the impurity. The two tunneling conductance channels interfere. The result is a tunneling density of states that can be described by a Fano lineshape (see [25]). The density of states is a dip in the case of dominant tunneling into the bound state, or a peak in the case of dominant tunneling into the free electron cloud, as schematically shown in Figure 1.4. The Fano anomaly occurs around single magnetic impurities. It has been studied by [26] and more recently in experiments with isolated molecules on metal surfaces by [27]. The Fano anomaly has been also observed in electronic systems having multiple bands crossing the Fermi level with very different effective masses, such as heavy fermions (see for example [28–30] or [31]).

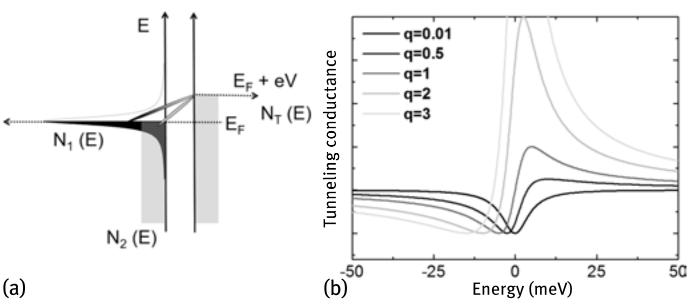

Fig. 1.4: In (a) we show a cartoon picture of the density of states of a band structure consisting of heavy (black) and light (light gray) bands in the sample (left side of the junction). Tunneling occurs from the tip (right side of the junction) which has a simple one band density of states. Eventually, tunneling can occur into each of the bands separately, in which case, there will be interference between tunneling into localized states and into the continuum. The result is a Fano anomaly, shown in (b). For this scheme, we use an energy width of the localized states of $\Gamma = 5$ meV and $E_0 = 0$ meV. The relative strength of tunneling into the resonant state is given by q. For large q, tunneling is into the resonant state, providing a near-Lorentzian shaped tunneling conductance. For low q, the phase shift due to tunneling into the resonant state produces destructive interference and a dip.

1.1.4 From tunneling into contact: Normal phase

When a normal metal tip is moved from tunneling distance to the sample, the wavefunctions overlap. Upon increasing the connection among both electrodes, there comes a point where the wavelike nature of transport is totally lost. Then, the conductance is given by Sharvin's formula which provides the tunneling conductance when transport is in the ballistic regime. Transport is classical, but the contact radius a is far below the electronic mean free path. In between, there is an interesting regime, where the conductance occurs just through a single atom. [32] showed that the chemical nature of the contacting atom determines the precise value of the conductance, which is a multiple of the quantum of conductance $\sigma_0 = \frac{2e^2}{h}$, with e being the electron charge and h Planck's constant (see for example [33] or [34]).

1.1.5 From tunneling into contact: Superconducting phase

Let us consider the situation where two electrodes made of the same superconducting material are slowly moved into contact at zero temperature. When both electrodes are separated in the tunneling regime, single quasiparticle tunneling is possible only for applied voltages larger than two times the superconducting gap of the electrodes (i.e., $eV > 2\Delta$, see Figure 1.5a). For voltages below 2Δ, Andreev reflection provides a conduction mechanism. It involves multiple crossings of the tunneling barrier, as we discuss below. Thus, the Andreev current is further exponentially suppressed with respect to the usual quasiparticle tunneling. The Andreev current is found using Bogoliubov equations, which are the equivalent of the Schrödinger equation for electrons in normal metals for superconductors (see for example the book by [35]).

In an S-S junction, the Andreev conduction mechanism implies multiple reflections through the junction. For $eV < 2\Delta$, electron-like excitations of electrode 1 cannot enter into the gap region of electrode 2 as a single quasiparticle. However, we can find a hole-like quasiparticle with opposite wavevector and spin in the same electrode. This produces a Cooper pair in electrode 2 and a current with $2e$ flows through the junction (Figure 1.5b). The hole-like quasiparticle is reflected into electrode 1 within the region of occupied electron-like states of electrode 1. This was first discussed by Blonder, Tinkham and Klapwijk (BTK) in experiments in macroscopic N-S junctions ([36]). The appendix of that paper shows the procedure needed to obtain the current-voltage

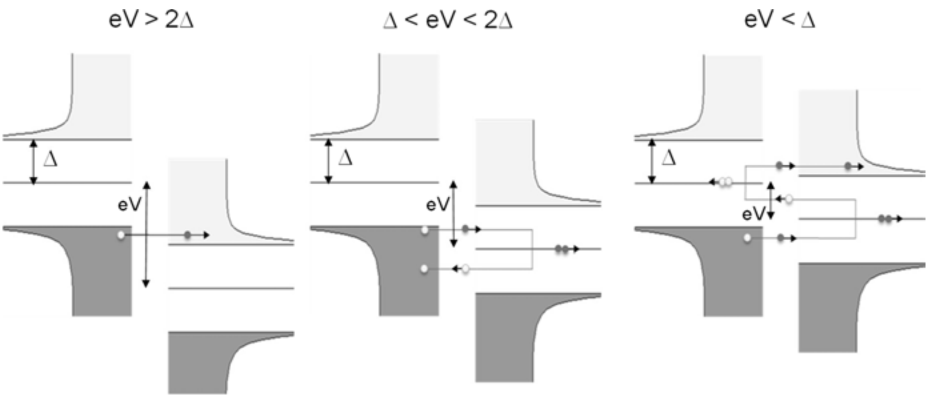

(a) Electrode 1 Electrode 2 (b) Electrode 1 Electrode 2 (c) Electrode 1 Electrode 2

Single quasiparticle tunneling process — Multiple quasiparticle tunneling via Andreev reflections

Fig. 1.5: In this image we show the behavior of a typical superconductor-superconductor junction when tip and sample are sufficiently close to show in-gap conductance. In (a) we show a single particle tunneling process for bias voltages above 2Δ. In (b) we show in-gap conductance due to a process crossing the tunneling barrier twice through Andreev reflection. In (c) we show the process crossing the tunneling barrier three times.

characteristics of N-S junctions for any tunneling barrier. An extension of the BTK formalism to superconductor-superconductor (S-S) junctions was later made by [37].

A more detailed analysis of the S-S situation takes into account all quasiparticle bound states. The formalism developed by [38, 39] leads to results that reproduce exactly the experimental observations in junctions involving a controlled amount of conduction channels. In Figure 1.5c we show schematically an example of multiple Andreev reflection processes. For $eV < 2\Delta$ multiple Andreev reflections occur in both electrodes 1 and 2. The smaller eV is compared to Δ, the larger is the number of Andreev reflections needed to obtain an Andreev current. For example, in the cases shown in Figure 1.5 we obtain one single quasiparticle transmitted in case (a), two in (b) – in the form of a Cooper pair, and three in (c) – in the form of a Cooper pair and an excited quasiparticle. For a current to flow from one junction to the other, the transmission probability must be multiplied at each barrier crossing. For a junction with transmission τ, the processes shown in Figure 1.5(b) and (c) have transmissions τ^2 and τ^3, respectively. Thus, unless τ is close to one, the contribution of Andreev reflection processes to the tunneling current is small. For a typical STM measurement in tunneling regime, with tunneling resistance of $10\,\mathrm{M}\Omega$, the transmission is about 10^{-3} ($\tau = (1/\sigma_0 \times 10\,\mathrm{M}\Omega)^{-1}$). It is thus difficult to observe Andreev reflection processes in the tunneling limit, although it is not impossible by measuring carefully enough and at short tip-sample distances, as discussed by [40].

With the STM we can control tip to sample distance, from high resistance tunneling conditions down to atomic contact between the electrodes (tip and sample). As the tip is moved towards the sample, the transmission through the tunnel barrier τ increases. In Figure 1.6 we present a series of current-voltage and conductance curves ($I - V$ and $dI/dV - V$) obtained when a Pb tip is moved towards a Pb sample. Similar results have been discussed by [34, 41]. We observe features in the curves for $V < 2\Delta$ when the resistance of the junction is decreased towards contact. Atomic contact is reached when the transmission equals a single quantum channel with spin degeneracy, $\tau = 1$, that is, when the resistance approaches the inverse of the quantum of conductance $1/\sigma_0 = R_Q = h/2e^2 = 12.9\,\mathrm{k}\Omega$.

For a single quantum channel, each value of the transmission τ is uniquely locked to a single current versus bias voltage curve. Thus, from the experimental curves we can obtain, with high precision, the number of quantum channels and their transmission τ_i, as first shown by [32].

The conductance curves shown in Figure 1.6 also present a feature at zero bias. This feature is the signature of the Josephson effect due to Cooper pair tunneling between both electrodes. [42] calculated the critical current of the Josephson junction I_C in a short constriction at zero temperature and found $I_C = (\pi\sigma_N\Delta)/2e$, where σ_N is the conductance of the junction in the normal state. Its value for quantum contacts with a small number of conducting channels was calculated by [43]. Available experiments provide T_C values smaller than expected in calculations that usually do not take into account the actual properties of the junction, namely thermal broadening,